Nano Research

Open Access

Review Article

Advanced micro-/nano additive manufacturing of multi-materials

Honghao Xiang[§], Zihan Xu[§], Haojie Lu ✉, and Mingchao Zhang ✉

Department of Materials Science and Engineering, National University of Singapore, Singapore 117575, Singapore
[§] Honghao Xiang and Zihan Xu contributed equally to this work.

Cite this article: *Nano Research*, **2026**, *19*, 94908451. https://doi.org/10.26599/NR.2026.94908451

ABSTRACT: Micro-/nano additive manufacturing (μnAM) is enabling three-dimensional architected structures with sub-micrometer features. Yet, a coherent view that links process platforms, multi-material design strategies, scale-dependent properties, and device performance is still emerging. This review consolidates recent progress in μnAM with an emphasis on its multi-material capabilities. We first outline the main technology families, spanning transformation-based assembly, micro powder-bed fusion, extrusion, jetting, and photopolymerization, and highlight their characteristic length scales, material windows, and throughput. We then compare strategies for combining polymers, metals, and inorganic non-metals, including template- and precursor-mediated routes as well as the directed assembly of nanoparticles and nanocrystals toward "any-material" voxel design. Building on this, we analyze how micro-/nanoscale architecture and interfaces govern mechanical, optical, interfacial, electrical, piezoelectric properties, and collective robotic behaviors, and map these structure–processing–property relationships onto emerging applications in optical devices, micro-/nano sensors, and micro-/nanorobots. Finally, we outline key challenges and research directions toward high-throughput, robust, and industrially relevant multi-material μnAM.

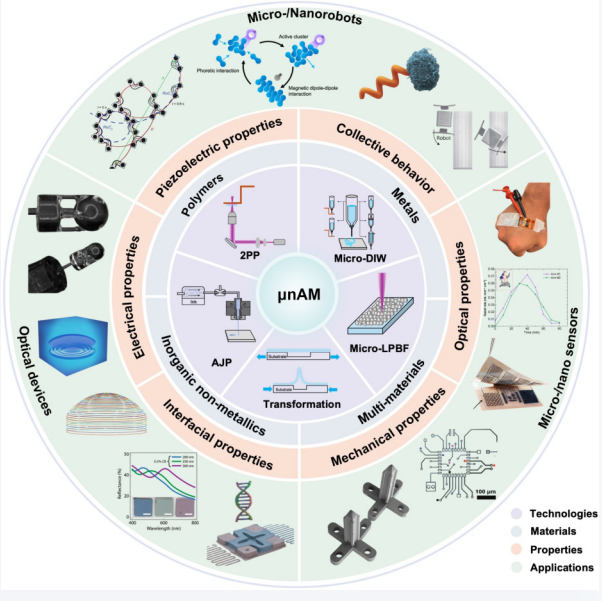

KEYWORDS: additive manufacturing, three-dimensional (3D) printing, micro-/nano scale, multi-materials, two-photon polymerization

1 Introduction

Additive manufacturing (AM), commonly known as three-dimensional (3D) printing, has advanced rapidly since its first commercialization in the 1980s [1], drawing sustained global interest from researchers. By building objects layer-by-layer directly from digital models [2], AM eliminates the dependence on conventional molds, cutting tools, and high-precision computer numerical control (CNC) machinery, dramatically expanding design freedom and enabling the fabrication of highly complex structures [3]. More recently, voxel-scale AM has shifted the paradigm from "layers" to "volumes," allowing material to be deposited precisely throughout 3D space and greatly improving both manufacturing efficiency and process controllability [4, 5].

As demand grows for miniaturized, multifunctional, high-performance devices, more requirements are imposed on micro-/nano-scale manufacturing [6, 7]. Conventional approaches rely heavily on photolithography, including ultraviolet, electron-beam, and ion-beam lithography [8], which remain unrivaled for high-throughput production of two-dimensional (2D) integrated-circuit patterns. However, these methods struggle with fully 3D, non-planar architectures and heterogeneous multi-material assemblies because of their reliance on masks, complex multi-step workflows, and strict clean-room conditions [9, 10].

Micro-/nano additive manufacturing (μnAM) provides a compelling alternative. Free from masks, it enables rapid, customizable 3D fabrication of multi-material structures, making it especially attractive for agile prototyping of complex geometries,

Received: December 8, 2025; **Revised:** January 13, 2026
Accepted: January 15, 2026

✉Address correspondence to Haojie Lu, luhj@nus.edu.sg; Mingchao Zhang, zhangmc@nus.edu.sg

functionally graded materials, and micro-devices. Consequently, μnAM has emerged as a vibrant frontier of current research.

Building on conventional AM technology [11], μnAM has progressed through optical-system refinements, miniaturized motion stages, and increasingly diverse material chemistries. According to their material-delivery mechanisms and forming principles, μnAM techniques can be grouped into transformation-based (2D-to-3D) assembly, powder-bed fusion, material extrusion, material jetting, and photopolymerization. Each category exhibits distinct characteristics and unique advantages in specific application scenarios [12].

Concurrently, the material palette for μnAM has expanded far beyond early single-polymer systems to encompass metals, inorganic ceramics, and hybrid multi-material combinations [13]. As 3D architectures miniaturize to micro- and nanoscales, they exhibit properties not observed in macroscopic counterparts, including enhanced mechanical performance, tailored optical responses, engineered surface interactions, high electrical conductivity, piezoelectric coupling, and collective behaviors in micro-/nanorobots. Advances in materials and the deliberate exploitation of these scale-dependent effects have broadened the application space of μnAM, enabling progress in photonic and optical devices, micro-/nano sensors, and micro-/nanorobots. The schematic illustration of the μnAM process is shown in Fig. 1.

Despite these advances, some key challenges remain: achieving micro-/nano dimensional accuracy, ensuring physicochemical compatibility at multi-material interfaces, and enhancing the interfacial bonding strength across disparate materials. Therefore, this review provides a systematic overview of current μnAM technologies and multi-material assembly strategies, representative properties, highlights representative advanced applications, analyzes persisting technical bottlenecks, and outlines future research directions toward translating μnAM from laboratory developments to industrial deployment.

2 μnAM technologies

2.1 Transformation-based technologies

Conventional 2D lithography offers unmatched advantages in

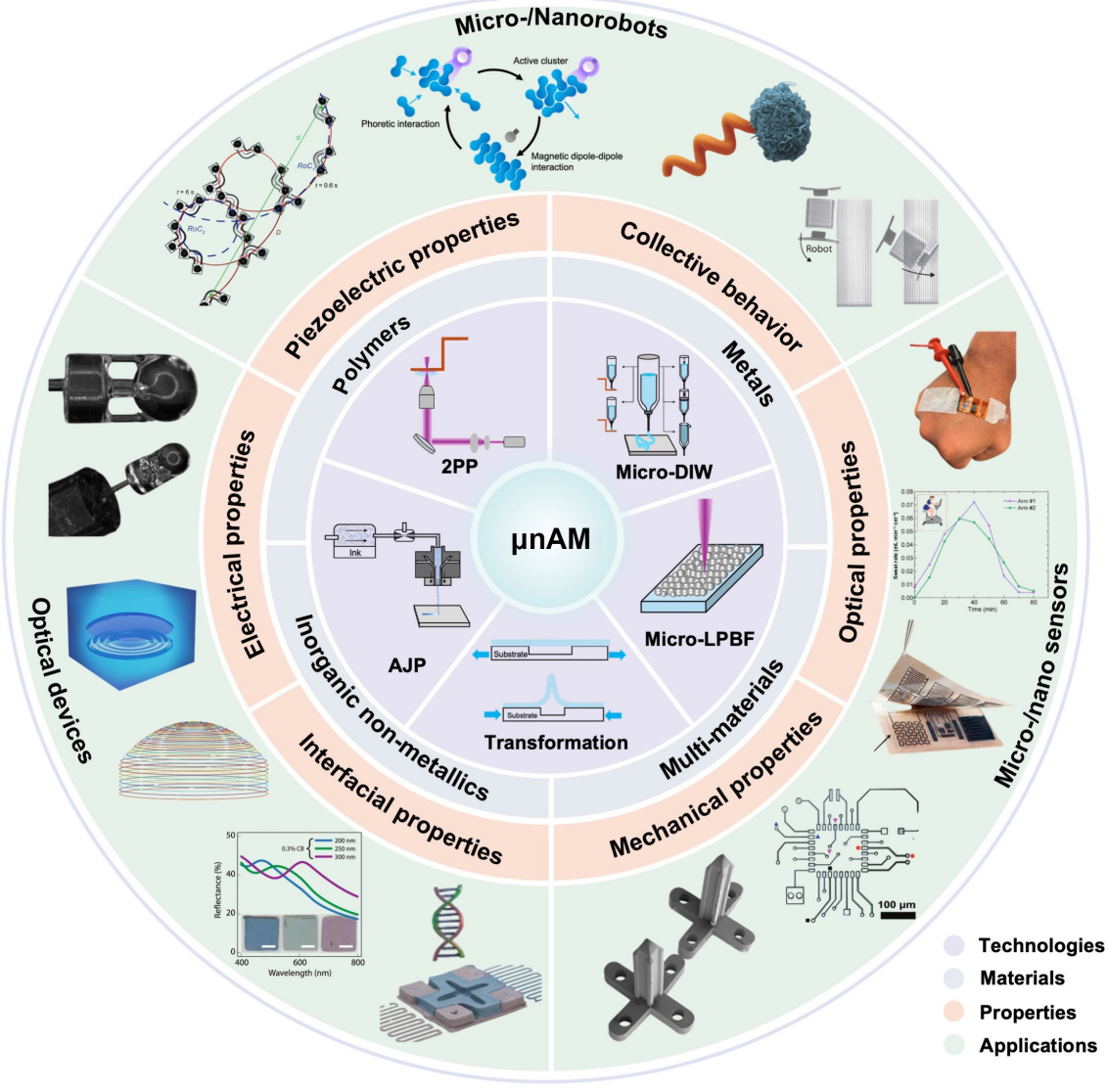

Figure 1 Schematic illustration of μnAM process: technologies, materials, properties, and applications. Micro-LPBF: micro laser powder bed fusion; Micro-DIW: micro direct ink writing; AJP: aerosol jet printing; 2PP: two-photon polymerization.

resolution, parallel fabrication, and wafer-scale throughput, making it a powerful platform for defining complex planar micro- and nano-architectures. By coupling such planar patterning with controlled deformation, transformation-based assembly provides an efficient route to 3D structures: Lithographically defined 2D precursors are converted into stereoscopic architectures through carefully designed templates and deformation pathways. In this section, we highlight deformation-guided strategies that leverage mature 2D lithographic processes to generate 3D micro- and nano-architectures across a broad range of length scales. The features of this method are listed in Table 1.

Using a lithography-based approach, Oliver G. et al. [14] showed that selective etching of an underlying sacrificial layer can release built-in strain, causing the overlying film to bend upward and roll into tubular 3D structures, particularly when the lattice constant of the top film exceeds that of the bottom layer (Fig. 2(a)). This method produced SiGe-based nanotubes with a minimum diameter of only 50 nm. In a mechanically induced strategy, Junseong Ahn et al. [15] patterned 2D structures on a pre-strained elastomeric substrate and subsequently released the pre-strain to trigger compressive buckling, transforming suspended regions into targeted 3D forms, as shown in Fig. 2(b). Recently, kirigami-inspired structures have become increasingly popular, transforming rigid thin sheets into highly flexible and stretchable structures through slit patterns [16]. Through geometric design, thin films can be reconfigured into complex out-of-plane 3D structures exhibiting tailored mechanical response [17].

Despite these advances, transformation-based methods remain largely limited to shrinking, rolling, folding, curving, and buckling [18, 19]. The routine fabrication of fully freeform, truly 3D nanostructures still require further breakthroughs in material design, process control, and multi-physics coupling.

2.2 Powder-bed-based technologies

While transformation-based strategies rely on pre-patterned planar films and subsequent mechanical transformation to achieve 3D geometries, powder-bed-based techniques build the architecture directly in three dimensions. They eliminate the 2D precursor entirely and instead consolidate discrete particles layer by layer. In particular, powder-bed fusion enables true additive consolidation of metals, and increasingly ceramics and composites, although its ultimate resolution is constrained by thermal transport, melt-pool dynamics, and powder statistics. The features of powder-bed-based technologies are listed in Table 1.

Powder-bed-based techniques involve first laying a thin layer of powder on a substrate, then sticking, sintering, or melting the powder together in a selected area to form a layer of cross-section, followed by repeated spreading and consolidation of subsequent powder layers to obtain a 3D solid [20, 21]. Among powder-bed processes, laser powder bed fusion (LPBF) is the only technique that routinely achieves micro-scale precision. Other techniques like binder jetting (BJ) are optimized for high throughput and large parts, so they are generally unsuitable for micro-scale precision.

LPBF, also called selective laser melting, is a principal metal AM process. A laser scans and melts a thin layer of metal powder to form each cross-section, and successive layers are fused to build the solid part, as shown in Fig. 2(c). Conventional LPBF typically uses a Gaussian laser beam with a spot diameter of about 80 μm [22], powder particles of 25–50 μm, and a layer thickness of 30 μm. In contrast, micro-LPBF reduces the beam diameter to less than 40 μm, the layer thickness to less than 10 μm, and the powder size to less than 10 μm [23], enabling the fabrication of micro-scale structures. However, miniaturization introduces several challenges, including increased surface roughness caused by particle adhesion at small spot sizes, strong van der Waals—driven agglomeration of

Table 1 Comparison of representative μnAM technologies

Classification	Techniques	Minimum resolution	Throughput	Compatible materials	Key advantages	Main limitations
Transformation-based	Lithographic and mechanically guided assembly methods	≈ 50 nm [14]	Very high	Thin films (Si/SiGe, metals via thin-film stacks)	High resolution and easy to achieve	Limited to folding, rolling, and buckling deformations
Powder-bed-based	Micro-LPBF	≈ 15 μm [27]	Medium	Metals	True 3D-printed metals with high density	Fine powders agglomerate and have limited thin-wall capability
Extrusion-based	Micro-DIW	≈ 100 μm [31]	Medium	Polymers, hydrogels, particle-filled inks, functional composites	Broad materials window and easy multi-material switching	Sensitive to ink's rheology and problems with clogging nozzles
	Micro-FDM	≈ 70 μm [36]	High	Thermoplastics	Simple, cheap, and robust	Interlayer bonding is weak and micro-nozzles could be clogged
Jetting-based	AJP	≈ 10 μm [38]	Low–medium	Metal nanoparticle inks, polymers, oxides	Broad viscosity tolerance and good for interconnects	Sensitive to airflow stability and limited volumetric 3D build
	EJP	≈ 10 μm [45]	Low	Conductive inks and solvents	Ultra-high resolution direct-write	Requires high voltage and is sensitive to temperature
	SPPW	≈ 10 μm [56]	Very high	Photopolymers	Extremely fast lattice structure fabrication	Not fully freeform 3D printing
Photopolymerization-based	PμSL	≈ 0.6 μm [61]	High	Photopolymers	Good balance of resolution, throughput, and build size	Layer-wise stair-stepping artifacts and light scattering in resins
	2PP	≈ 100 nm [67]	Low	Photopolymers	True freeform 3D printing with nanoscale resolution	Long printing time and high cost of the equipment

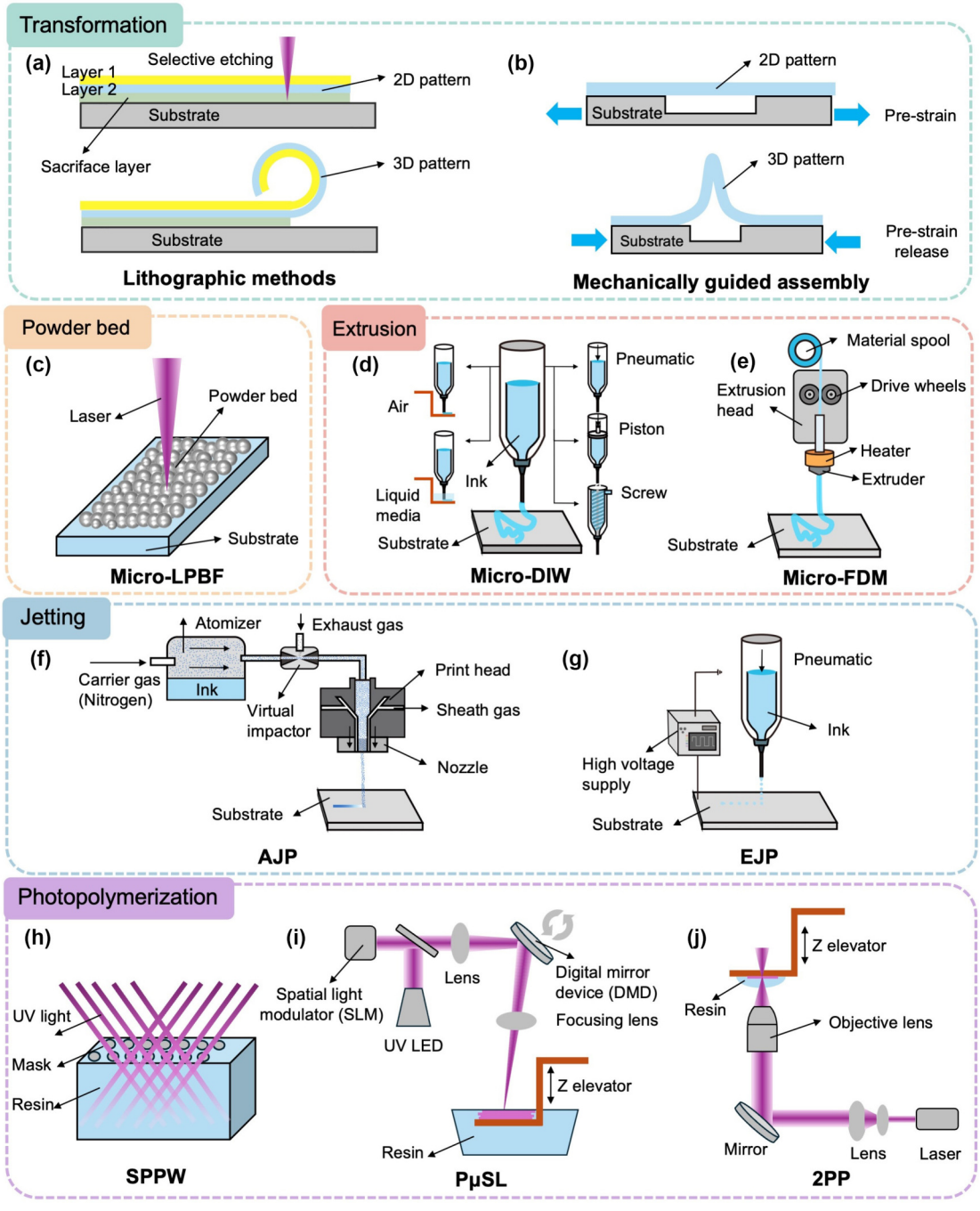

Figure 2 Schematic illustrations of μnAM technologies. (a) Transformation-based lithographic methods. (b) Transformation-based mechanically guided assembly methods. (c) Micro laser powder bed fusion (Micro-LPBF). (d) Micro-DIW. (e) Micro-FDM. (f) AJP. (g) EJP. (h) SPPW. (i) PμSL. (j) 2PP.

fine powders, microstructural instabilities, and elevated residual stress. Recent studies to address these issues include the use of continuous-wave lasers [23], improved powder-spreading strategies [24], and rigorous process-parameter optimization [25, 26].

State-of-the-art micro-LPBF has reported a minimum feature size of 15 μm, surface roughness as low as 1 μm, and part density up to 99.3% [27]. Nevertheless, the routine fabrication of arbitrary micrometer-scale and especially nanometer-scale thin-walled metal structures remains an open challenge.

2.3 Extrusion-based technologies

In contrast to powder-bed fusion, which relies on the spreading and selective consolidation of discrete particles, extrusion-based methods deliver material in a continuous manner through a nozzle. These methods broaden the accessible material palette and simplify tooling compared to powder-bed fusion. Nonetheless, filament diameter, nozzle wear, and thermal or rheological limits still constrain the achievable resolution. The features of extrusion-based technologies are listed in Table 1.

2.3.1 Micro direct ink writing (Micro-DIW)

DIW is a comparatively accessible AM method. In DIW, an ink with tailored rheology is extruded from a syringe barrel, forms a continuous filament at the nozzle, and is deposited layer by layer

along a prescribed toolpath to build a 3D structure [28]. DIW extrusion methods are mainly classified into pneumatic, piston-based, and screw-based, as shown in Fig. 2(d). The approach is low-cost and compatible with a wide range of materials [29, 30]. However, its resolution and dimensional accuracy are typically limited to a few hundred micrometers to several millimeters. In recent years, advances in nozzle miniaturization, high-precision flow control, and ink formulation have reduced line widths below 100 μm [31], enabling micro-DIW.

However, shrinking the nozzle introduces many new challenges. Accurate volumetric flow control becomes difficult at small scales; ink compressibility and non-uniformity can degrade print stability; transient extrusion dynamics deviate from ideal behavior; complex, frequently non-Newtonian ink rheology complicates process tuning; and ink properties are highly sensitive to temperature [32]. These factors collectively limit reliable micro-/nanoscale patterning, indicating that further progress will require co-optimization of hardware, control strategies, and ink chemistries.

2.3.2 *Micro fused deposition modeling (Micro-FDM)*

FDM is a widely adopted AM method that typically processes thermoplastics such as acrylonitrile–butadiene–styrene (ABS) and polylactic acid (PLA) [33]. During printing, the filament is heated and melted at the nozzle, extruded, and deposited layer by layer onto a cooler build platform to form a 3D object [34], as shown in Fig. 2(e). Commercial systems generally achieve only about 250 to 300 μm in dimensional accuracy [35], which is insufficient for micro-scale fabrication.

Several studies have addressed these limits by refining hardware and process parameters. Quero et al. [36] reported a lateral accuracy of 70 ± 11 μm via optimizing nozzle geometry, machine frame, platform rigidity, layer height, and extrusion width. They emphasized that nozzle shape strongly influences thermal radiation and, in turn, the attainable feature size. Despite this progress, advancing FDM into micrometer-scale fabrication remains difficult. Micro nozzles are more susceptible to wear and clogging, which narrows the usable material library. Thermal management becomes more challenging; rapid filament cooling reduces interlayer welding strength and lowers throughput [37].

2.4 Jetting-based technologies

To further push feature sizes below those typically achievable by extrusion, material delivery can shift from continuous filaments to discrete droplets. Jetting-based methods dispense picoliter-to-nanoliter droplets through nozzles, enabling finer lines than conventional extrusion while retaining considerable material versatility. Environmental sensitivity and modest printing speed, however, restrict their role in building larger-volume 3D structures. The features of jetting-based technologies are listed in Table 1.

2.4.1 *Aerosol jet printing (AJP)*

AJP is an advanced direct-write AM technique for micro- and nano-scale fabrication. The process atomizes functional inks into aerosol droplets and aerodynamically focuses them onto a substrate, enabling nanometer-thick deposits and micrometer-scale features with resolutions down to about 10 μm [38]. A schematic of the process is shown in Fig. 2(f). AJP is highly materials-versatile, accommodating metallic nanoparticle inks, polymers, biomaterials, and semiconducting oxides [39–41], with almost no restrictions imposed by ink viscosity.

The method also has limitations. Throughput is relatively low, and printing accuracy is sensitive to airflow stability and ink rheology, so the attainable resolution can degrade under suboptimal conditions [42]. Even so, AJP has been widely applied to biosensors, microdevices, and flexible electronics, and it supports direct printing of interconnects and other circuit elements [43]. Its combination of fine resolution, non-contact deposition, and broad materials compatibility underscores strong potential for micro-/nano-scale manufacturing.

2.4.2 *Electrohydrodynamic jet printing (EJP)*

EJP applies a high electric field, typically from a few hundred to several thousand volts, between a nozzle and a substrate. This field shapes the meniscus into a Taylor cone and draws out a fine jet, producing minute liquid columns or droplets for direct writing [44], as shown in Fig. 2(g). Using this mechanism, EJP routinely achieves line widths and patterned features below 10 μm and, under favorable conditions, below 1 μm [45]. Resolution can be tuned by adjusting ink rheology and conductivity, voltage and waveform, nozzle diameter, electrode spacing, and ambient conditions such as humidity and temperature.

EJP printing offers very high resolution and broad ink compatibility. Relative to aerosol jet printing, it is well suited to flexible substrates and does not require stencils [46–48]. Its limitations include modest throughput, strong sensitivity to environmental fluctuations, and generally limited compatibility with biological substrates due to high electric fields and solvent requirements. Current applications span flexible electronics, sensors, biomedical interfaces, and the fabrication of microdevices and microstructures [49, 50].

2.5 Photopolymerization-based technologies

Jetting thus occupies a niche where fine features and multi-material capability are prioritized over build speed and volume. To further decouple resolution from nozzle diameter and ink rheology, material delivery can be shifted from physical extrusion or jetting to optically defined solidification. Photopolymerization-based techniques use patterned light to localize curing within liquid photoresists: Self-propagating photopolymer wave (SPPW) and projection micro-stereolithography (PμSL) extend lithography into 3D but remain fundamentally layer-defined or mask-constrained, whereas two-photon polymerization (2PP) writes directly inside the volume with sub-diffraction voxels, enabling true 3D free-form control at the nanoscale. The features of photopolymerization-based technologies are listed in Table 1.

2.5.1 *Self-propagating photopolymer wave*

SPPW lithography illuminates a patterned photomask with one or more collimated ultraviolet (UV) beams. The resulting light field forms a self-guided optical wave inside the photoresist, which locally cross-links the material along the waveguide path [51, 52]. The schematic diagram of SPPW is shown in Fig. 2(h).

This approach elevates photolithography from a planar 2D process to a volumetric 3D process and enables rapid fabrication of 3D microarchitectures. SPPW is not regarded as a full 3D-printing technique because it cannot easily produce smoothly curved surfaces. However, careful mask design together with precise control of the incident-beam angle allows the construction of complex unit cells and truss-based lattices [53] in less than one minute [54]. Feature sizes are highly tunable, unit-cell dimensions

range from 0.1 mm to more than 10 mm [55], and individual truss diameters can be adjusted between 0.01 and 1 mm [56].

2.5.2 *Projection micro-stereolithography*

PμSL evolved from traditional stereolithography (SLA) technology [57]. A typical PμSL system uses a digital micromirror device (DMD) to project 2D patterns onto a photosensitive resin [58]. Each layer is solidified in a single exposure, and successive layers are stacked to build the complete structure. This layer-wide exposure greatly increases fabrication speed and throughput compared with conventional point-by-point SLA laser scanning [59, 60]. A schematic illustration of PμSL is provided in Fig. 2(i).

In addition to the DMD system, a spatial light modulator (SLM) can dynamically modulate the phase and amplitude of the light field to realize advanced beam shaping, focus control, and adaptive exposure patterns. This variant is often termed large-area projection micro-stereolithography (LAPμSL) [59, 61]. Combined with high-resolution optics and micro-/nano-scale motion stages, feature size can be precisely controlled by adjusting exposure time, light intensity, pixel grayscale value, and resin absorbance [62]. Ongoing development and commercialization have improved performance and lowered costs, making PμSL well-suited for complex geometries and establishing it as a core technique in micro-scale AM technology [61].

2.5.3 *Two-photon polymerization*

2PP represents a breakthrough in μnAM, fundamentally distinct from single-photon methods such as SLA and PμSL. The process relies on a nonlinear optical effect: A tightly focused femtosecond laser induces two-photon absorption within a photosensitive resin (Fig. 2(j)) [63]. Only at the focal point is the photon flux high enough for two-photon absorption to occur: only when two photons are absorbed almost simultaneously at this focus are free radicals generated, initiating polymer chain growth and cross-linking that are thus confined to the focal volume [64, 65]. This mechanism allows 2PP to break the diffraction limit [66], enabling theoretical feature sizes below 100 nm and even manufacturing objects with structural dimensions of tens of nanometers [67]. In practice, the smallest voxel size and feature fidelity are jointly governed by the resist's threshold behavior (initiator efficiency, radical diffusion, and monomer reactivity), shrinkage and cross-linking density, as well as optical and processing parameters such as numerical aperture, wavelength, pulse energy, scan speed, and repetition rate.

Nanoscribe GmbH was the first company to commercialize 2PP, offering high-resolution printers and tailor-made photoresists (IP-Dip, IP-L 780, IP-S, etc.) [68]. True nanoscale 3D printing opens new avenues for nanotechnology, giving researchers unprecedented design freedom. As a result, 2PP is rapidly gaining traction in areas such as micro-robotics, biomedical microdevices, and micro-optoelectronics, where ultra-fine, complex freeform architectures are essential [69, 70].

3 Multi-materials and process strategies

3.1 Polymers

Polymers are exceptionally well-suited for μnAM because many can be processed at room or modest temperatures, feature highly tunable chemical structures, and exhibit rheological properties that can be engineered for specific printing platforms. They can be rapidly cured and patterned, and their properties are readily modulated by external stimuli, such as light, heat, electric fields, or solvent environments. These attributes make polymers ideal candidates for μnAM, where they serve not only as lightweight structural scaffolds but also as versatile functional matrices in multi-material architectures.

Thermoplastics constitute an important class of μnAM feedstocks owing to their melt-processability, mechanical robustness, and broad availability in biocompatible and biodegradable formulations [71]. They are particularly compatible with extrusion-based techniques. Figure 3(a) shows the microstructure of PLA produced by Yamada et al. [72] using micro-FDM, with lateral and depth resolutions of 40 and 45 μm, respectively. Although this accuracy is lower than that achievable with photopolymers, thermoplastics offer important advantages: They are generally non-toxic, biodegradable (in the case of PLA), and easy to process, with melt viscosity and crystallinity that can be tailored through molecular weight and copolymer composition. Their good mechanical stability, thermal resistance, and widespread availability also make thermoplastics attractive as structural materials or bulk supports in μnAM, especially where cost, biocompatibility, and recyclability are prioritized over sub-micron resolution.

In contrast to melt-processable thermoplastics which are shaped by heating and cooling, photopolymers are solidified directly by light. Photopolymers undergo light-induced chain growth, most commonly via free-radical photopolymerization, in which irradiation generates reactive species that drive monomers to form cross-linked polymer networks [73]. Representative systems are based on acrylate or methacrylate esters, such as poly(ethylene glycol) diacrylate (PEGDA), ethoxylated bisphenol A dimethacrylate (Bis-EMA), trimethylolpropane triacrylate (TMPTA), and ethoxylated trimethylolpropane triacrylate (ETPTA) [74], used in combination with photoinitiators including ethyl (2,4,6-trimethylbenzoyl)phenylphosphinate (TPO-L), phenylbis (2,4,6-trimethylbenzoyl)phosphine oxide (Irgacure 819), and bis(2,4,6-trimethylbenzoyl)phenylphosphine oxide (BAPO) [75]. Solidification occurs within the laser-irradiated region, which makes these resins suitable for SPPW, PμSL, and 2PP. For example, Liu et al. [76] used 2PP to fabricate a Merlion lattice with lattice constants of 0.9–1.5 μm that exhibited structural color even slightly above the subwavelength regime (Fig. 3(b)), demonstrating the strong potential of photopolymers for micro-/nano-scale fabrication. It is also worth noting that Fischer et al. [66] emphasized that achieving nanoscale resolution in 3D resolution depends strongly on the photopolymer chemistry rather than optical system alone, underscoring the need for continued materials development.

Beyond conventional, often hydrophobic, photopolymers, water-swollen polymer networks represent another important sub-class of light-processable materials. Hydrogels possess good hydrophilicity and biocompatibility, which have led to widespread use in soft robotics, implantable devices, and biomedical applications [77]. Torgersen et al. [78] employed 2PP to fabricate a micron-scale hydrogel scaffold (Fig. 3(c)), which supported the attachment of *C. elegans*, highlighting their excellent biocompatibility.

Beyond passive structural networks, stimuli-responsive functional polymers offer active control over shape and properties. Functional polymers, such as liquid-crystal elastomers (LCEs),

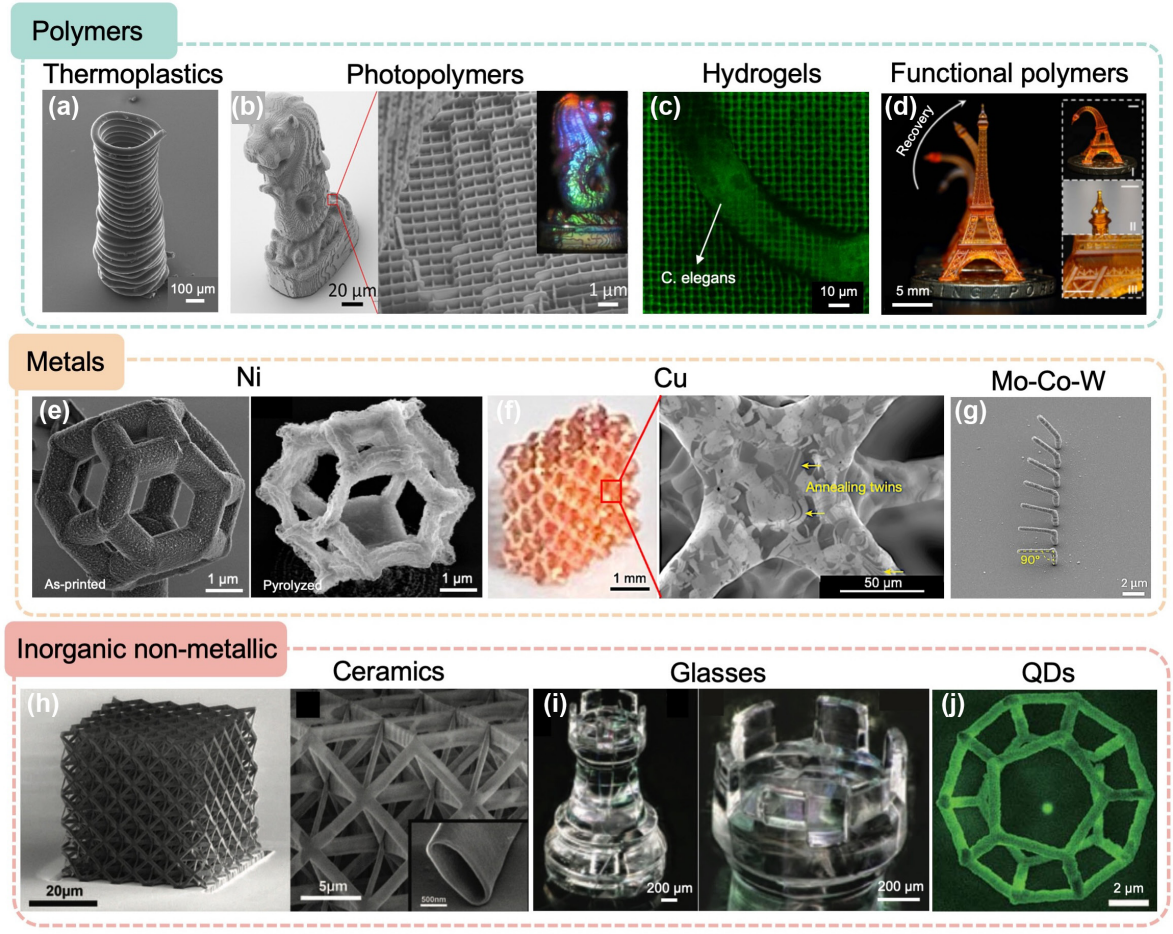

Figure 3 Representative μnAM examples across material classes. (a) Thermoplastic part fabricated by micro-FDM. Reproduced with permission with Ref. [72], © IOP Publishing Ltd 2008. (b) Photopolymer Merlion printed by 2PP, exhibiting structural color. Reproduced with permission with Ref. [76], © American Chemical Society 2022. (c) Microscale hydrogel network produced by 2PP with *Caenorhabditis elegans* (*C. elegans*) positioned on the scaffold. Reproduced with permission with Ref. [78], © SPIE 2012. (d) Functional shape-memory polymer structures fabricated by PμSL. Reproduced with permission with Ref. [80], © Ge, Q. et al. 2016. (e) Ni microstructures obtained by 2PP followed by pyrolysis. Reproduced with permission with Ref. [83], © Vyatskikh, A. et al. 2018. (f) Cu architectures printed by high-precision DLP and exhibiting annealed twin microstructures. Reproduced with permission with Ref. [88], © Saccone, M. A. et al. 2022. (g) Mo-Co-W features formed by *in situ* capture and deposition using 2PP. Reproduced with permission with Ref. [89], © Wang, Y. Y. et al. 2024. (h) Ceramic coating deposited by ALD on a 2PP-printed scaffold. Reproduced with permission with Ref. [92], © American Association for the Advancement of Science 2014. (i) Silica glass structures printed by 2PP and subsequently sintered. Reproduced with permission with Ref. [96], © Kotz, F. et al. 2021. (j) Cathodoluminescent QD architectures formed by 2PP-induced *in situ* crosslinking. Reproduced with permission with Ref. [100], © Liu, S. F. et al. 2022.

shape-memory polymers (SMPs), and photochromic or thermochromic systems [79], allow programmable deformation, photothermal response, and electro-optic control at the micro-/nanoscale, providing a foundation for micro-actuators and tunable optical components. For example, Fig. 3(d) shows SMP structures fabricated by Ge et al. [80] using PμSL that achieve complete shape recovery upon heating.

3.2 Metals

While polymers currently dominate μnAM owing to their processability and functional tunability, many target applications, such as high-strength micro-lattices, electrically conductive interconnects, and thermally stable components, ultimately demand metallic architectures. Direct fabrication of metals at the micro-/nanoscale remains challenging [81]. Despite substantial progress in micro-PBF, a significant gap persists between current capabilities and the routine production of defect-free micro-/nano-metal architectures [82].

Existing strategies for micro-/nanoscale metallic architectures generally fall into two categories. The first is precursor-loaded printing. Metal salt precursors are mixed with a photoresist, followed by printing the composite and subsequent pyrolysis and reduction of the organic matrix to yield a metal framework. For example, Vyatskikh et al. [83] produced Ni microstructures by this route (Fig. 3(e)). However, this strategy typically suffers from pronounced volumetric shrinkage, pore formation, and cracking during pyrolysis and reduction, which complicate dimensional control and defect-free fabrication.

The second is template-assisted metallization. A polymer template is fabricated by a photopolymerization-based technique, then conformally coated with a nanometric metal layer via chemical vapor deposition [84], electroless plating [55, 59, 60, 85, 86], or magnetron sputtering [81, 87]. Subsequent removal of the polymer by high-temperature calcination or O_2 plasma leaves a thin-walled metallic shell. However, this approach intrinsically yields hollow structures with limited wall thickness, which can suffer from mechanical fragility, non-uniform shell growth on complex

geometries, and collapse or distortion during template removal and thermal treatment. To overcome these limitations, several strategies aim to directly convert the template that has reacted with metal precursors into a dense metallic architecture. One representative approach uses hydrogel templates: Saccone et al. [88] first printed hydrogel scaffolds, then immersed them in metal-ion precursor solutions so that the ions chelate with functional groups in the hydrogel network, followed by calcination and reduction to obtain a dense Cu structure. The grains' microstructures can also be clearly observed (Fig. 3(f)), and this approach mitigates issues associated with hollow shells and shrinkage-induced collapse, providing a mechanically more robust metallic framework.

In parallel, several *in situ* metallization methods have emerged. Wang et al. [89] exploited optical trapping within the 2PP focus to locally decompose metal precursors and capture metal nanoclusters, directly forming Mo-Co-W microstructures (Fig. 3(g)). Cao et al. [90] achieved Ag features with minimum sizes near 180 nm by laser-induced reduction in solution. Jung et al. [91] printed Ag structures with hundreds of nanometers feature sizes directly using AJP. Although such *in situ* growth strategies are promising, their applicability is tightly constrained by precursor chemistry, reduction kinetics, and mass transport, and they are therefore currently limited to a relatively narrow set of metals.

3.3 Inorganic non-metallic materials

Beyond metals, many functional μnAM applications, such as high-temperature microdevices, optical components, and chemically robust scaffolds, require ceramics, glasses, and other inorganic non-metallic materials with superior hardness, thermal stability, and dielectric, piezoelectric, or optical performance. The fabrication of inorganic non-metallic materials can likewise be categorized into polymer-template routes and sintering-based routes. Ceramics represent a major class of inorganic non-metallic materials and have been studied extensively. Meza et al. [92] first printed a polymer scaffold by 2PP, then deposited tens of nanometers of Al_2O_3 by atomic layer deposition (ALD), and finally removed the polymer by O_2 plasma to obtain a thin-walled ceramic lattice (Fig. 3(h)). Vyatskikh et al. [93] synthesized titanium-containing monomers via ligand exchange between a titanium alkoxide and an acrylic acid framework, printed the composite, and then sintered and oxidized it to yield TiO_2 ceramic microstructures with promising photocatalytic performance. Zheng et al. [60] dispersed 150 nm Al_2O_3 nanoparticles (NPs) into a resin and printed the composite by PμSL, followed by sintering to obtain dense Al_2O_3 lattices. Sänger et al. [94] reported a similar strategy using yttria-stabilized zirconia (YSZ) particles. Printing by 2PP and subsequent sintering produced ceramic features with resolutions down to 500 nm, and the compressive strength exceeded that of bulk YSZ.

Silica glass (SiO_2) is another important inorganic material, especially for micro-optics [95]. Kotz et al. [96] dispersed amorphous silica NPs with a diameter of about 40 nm into a resin and selected a crosslinker to match the refractive index of the binder to that of fused silica. Printing by 2PP followed by sintering produced glass structures with feature sizes of tens of micrometers and surface roughness $R_a \approx 6$ nm (Fig. 3(i)). Wen et al. [97] formulated inks from PEG-functionalized, well-dispersed colloidal silica NPs and two small-molecule acrylates, then printed by 2PP to obtain silica glass with sub-200 μm resolution. Through doping and co-doping, rare-earth ions, Er^{3+}, Tm^{3+}, Yb^{3+}, Eu^{3+}, and Nd^{3+}, were incorporated directly into the printed SiO_2, yielding strong photoluminescence at target wavelengths. Cooperstein et al. [98] similarly demonstrated microscale yttrium aluminum garnet (YAG) doped with Nd^{3+}.

In parallel, the integration of quantum dots (QDs) into micro- and nano-devices has become an active research area [99]. Liu et al. [100] reported a method to pattern QD frameworks in their native composition. Photoexcitation generated electron-hole pairs that modified surface chemistry and promoted direct interparticle bonding, which enabled the printing of arbitrary 3D QD architectures with resolution beyond the diffraction limit. Cathodoluminescence images of the printed QDs structures are shown in Fig. 3(j).

3.4 Multi-materials

Although a wide range of individual materials, such as polymers, metals, and inorganic non-metallic materials, can be fabricated using the methods outlined above, most techniques remain largely material-specific and often introduce defects such as hollow shells or shrinkage-induced collapse, which hinder truly direct, 3D volumetric, "any-material" μnAM. Consequently, recent efforts have shifted towards more universally compatible approaches that exploit physical and chemical interactions to organize NPs or nanocrystals (NCs) [101] with high precision, thereby enabling arbitrary multi-material μnAM.

For example, Issa et al. [102] demonstrated electrostatic assembly of NPs. Acrylic monomers in a photoresist were functionalized with amine groups and cross-linked by 2PP to form positively charged microstructures. Carboxyl-terminated, negatively charged NPs then assembled onto the polymer surface via electrostatic attraction (Fig. 4(a)), permitting multi-material integration of Au, Fe_2O_3, and QDs (Figs. 4(b)–4(d)). Oran et al. [103] and Han et al. [104] leveraged hydrogen bonding. The 2PP process locally modified poly(acrylate-co-acrylamide) hydrogel networks in pure water to expose hydrogen-bonding sites at designated locations (Fig. 4(e)), after which diverse NPs were deposited (Figs. 4(f)–4(g)). They further introduced a hydrogel-shrink strategy that reduced linear dimensions by about tenfold, achieving effective feature sizes near 20 nm (Fig. 4(h)), below the limits of commercial 2PP systems.

Another route is to modify the surfaces of NCs by grafting cross-linkable ligands. Li et al. [105] reported direct covalent linking of NCs under 2PP. A small amount of a diazonium compound (BTO) was added to NC dispersions. Femtosecond laser irradiation generated nitro radicals at both ends of BTO, which formed covalent bonds with NC surfaces (Fig. 4(i)), enabling solid structures to be written directly along the laser path. This chemistry is broadly material-agnostic and was used to pattern metals, inorganics, and QDs at nanoscale resolution (Figs. 4(j) and 4(k)).

Exploiting the physical interaction of NPs can provide more universally compatible strategies. Lyu et al. [106] utilized non-specific capillary forces for NP capture. Substrates were selectively silanized to render them hydrophobic, while 3D templates remain hydrophilic. When these templates were repeatedly infiltrated into and withdrawn from NP dispersions (Fig. 4(l)), capillary forces at the receding meniscus drove NPs into and onto the hydrophilic templates. After solvent evaporation, the NPs were deposited layer by layer onto the templates (Figs. 4(m)–4(o)). Using this universal, physical-field-based approach, Au, Fe_3O_4, Pt, and $BaTiO_3$ were assembled onto polymer scaffolds.

Collectively, these studies underscore a growing shift toward "any-material" μnAM enabled by field-guided NP/NC assembly.

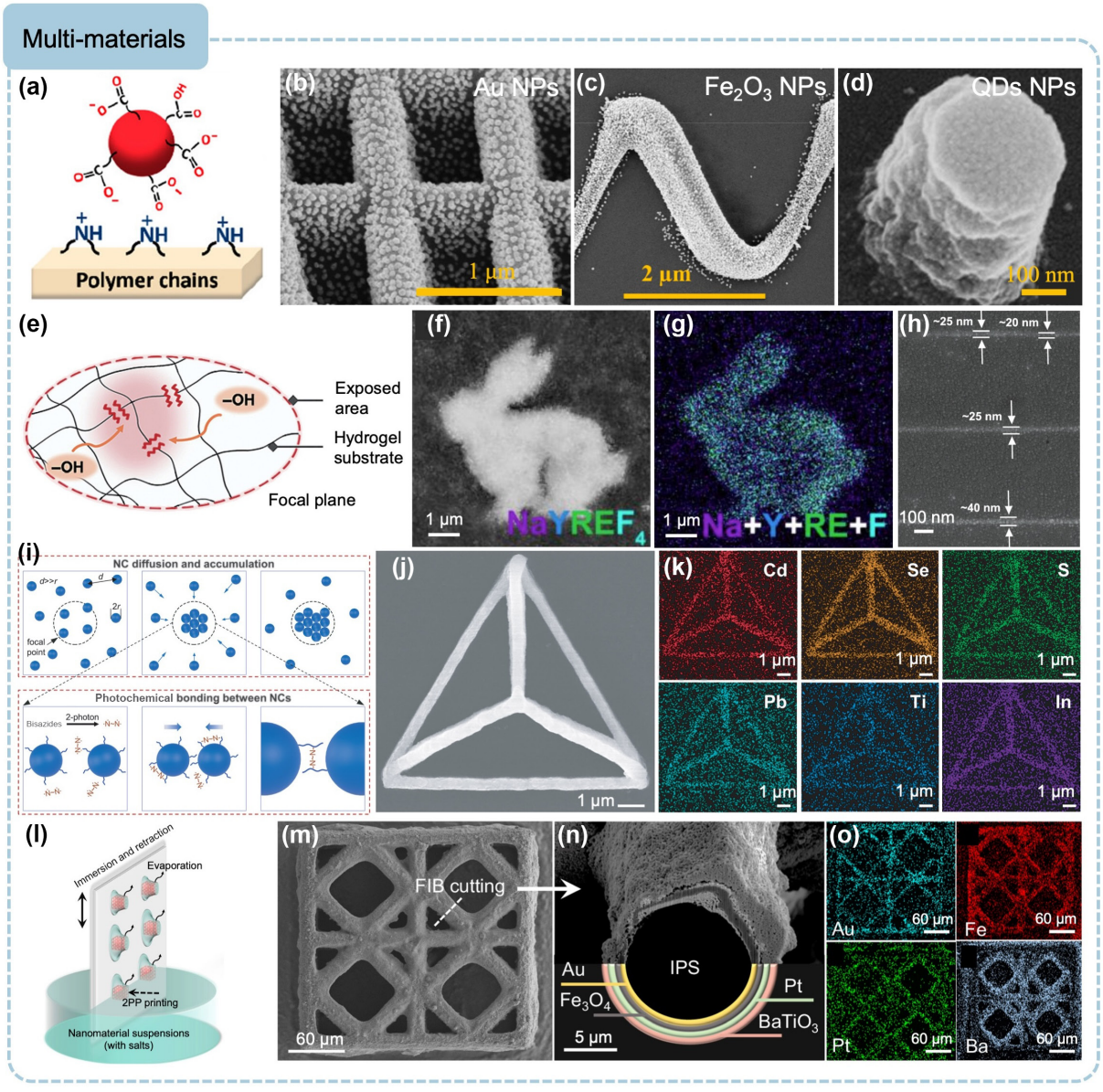

Figure 4 Representative examples of multi-material μnAM. (a) Schematic of electrostatic assembly of NPs. (b) Assembly of Au NPs. (c) Assembly of Fe_2O_3 NPs. (d) Assembly of QD NPs. Reproduced with permission with Ref. [102], © American Chemical Society 2021. (e) Schematic of hydrogen-bond-mediated NP assembly. (f) Assembly of $NaYREF_4$ (RE = Yb, Er, Tm, Gd, Mn, Lu) NPs. (g) Energy-dispersive X-ray spectroscopy maps of $NaYREF_4$ NP assembly. (h) Structures after hydrogel shrinking. Reproduced with permission with Ref. [104], © Han, F. et al. 2022. (i) Schematic of direct covalent linking of NCs. (j) Hybrid pyramidal framework printed from CdSe/ZnS, PbS, In_2O_3, and TiO_2 NCs. (k) EDS maps of the hybrid pyramidal framework. Reproduced with permission with Ref. [105], © Li, F. et al. 2023. (l) Schematic of capillary-force-driven NP capture. (m) Structure after sequential deposition of four materials. (n) Cross-section of a beam showing Au, Fe_3O_4, Pt, and $BaTiO_3$ from inner to outer layers. (o) EDS maps of the four elements. Reproduced with permission with Ref. [106], © Lyu, X. et al. 2024.

Although a number of promising chemistries and physical interactions have been demonstrated, truly broad and universally applicable interaction frameworks are still lacking and remain an important target for future research.

4 Micro-/nanoscale-specific properties

3D architectures at the micro-/nanoscale do more than alter geometry; they endow materials with physical responses that are difficult or impossible to realize in bulk form. Through μnAM and multi-material processing strategies, structural size, composition, and morphology can be precisely programmed, enabling new classes of materials and devices with enhanced mechanical performance, tailored photonic response, extreme wettability, high conductivity, and even emergent, swarm-like behaviors. These miniaturization-enabled properties substantially expand the design space for microsystems, biomimetic devices, flexible electronics, and intelligent robotics.

4.1 Mechanical properties

μnAM enables micro-/nano lattice materials in which reduced flaw sizes and densities push strength toward ideal limits. As a result, these lattices can surpass the conventional trade-offs that constrain bulk materials [107]. By tailoring unit-cell topology, wall thickness, and hierarchical organization, μnAM micro-/nano-lattices can also be engineered for energy absorption, damage tolerance, and

recoverable deformation, offering mechanically robust architectures that are inaccessible in monolithic bulk solids.

Zheng et al. [60] fabricated polymer (Fig. 5(b)), hollow Ni–P (Fig. 5(c)), hollow Al_2O_3 (Fig. 5(d)), and solid Al_2O_3 (Fig. 5(e)) lattices. The mechanical response differed markedly from that of monolithic counterparts: as density dropped by orders of magnitude, the stiffness-to-mass ratio remained comparatively high (Fig. 5(a)). Meza et al. [92] reported hollow ceramic microlattices that are ultralight, strong, and energy-absorbing, with recoverable deformation exceeding 50% compressive strain, thereby overcoming the brittleness and defect sensitivity of traditional ceramics. Bauer et al. [108] analyzed polymer-ceramic microlattices and found compressive strengths up to 280 MPa at densities well below 1000 kg·m^{-3}. These advances highlight μnAM lattices as candidates for application spaces that demand high specific stiffness and energy absorption.

4.2 Optical properties

μnAM opens routes to micro-/nano photonics, notably enabling the direct or indirect fabrication of photonic crystals that exhibit band gaps and structural color determined by lattice periodicity [109]. When feature sizes are miniaturized to sub-micrometer and

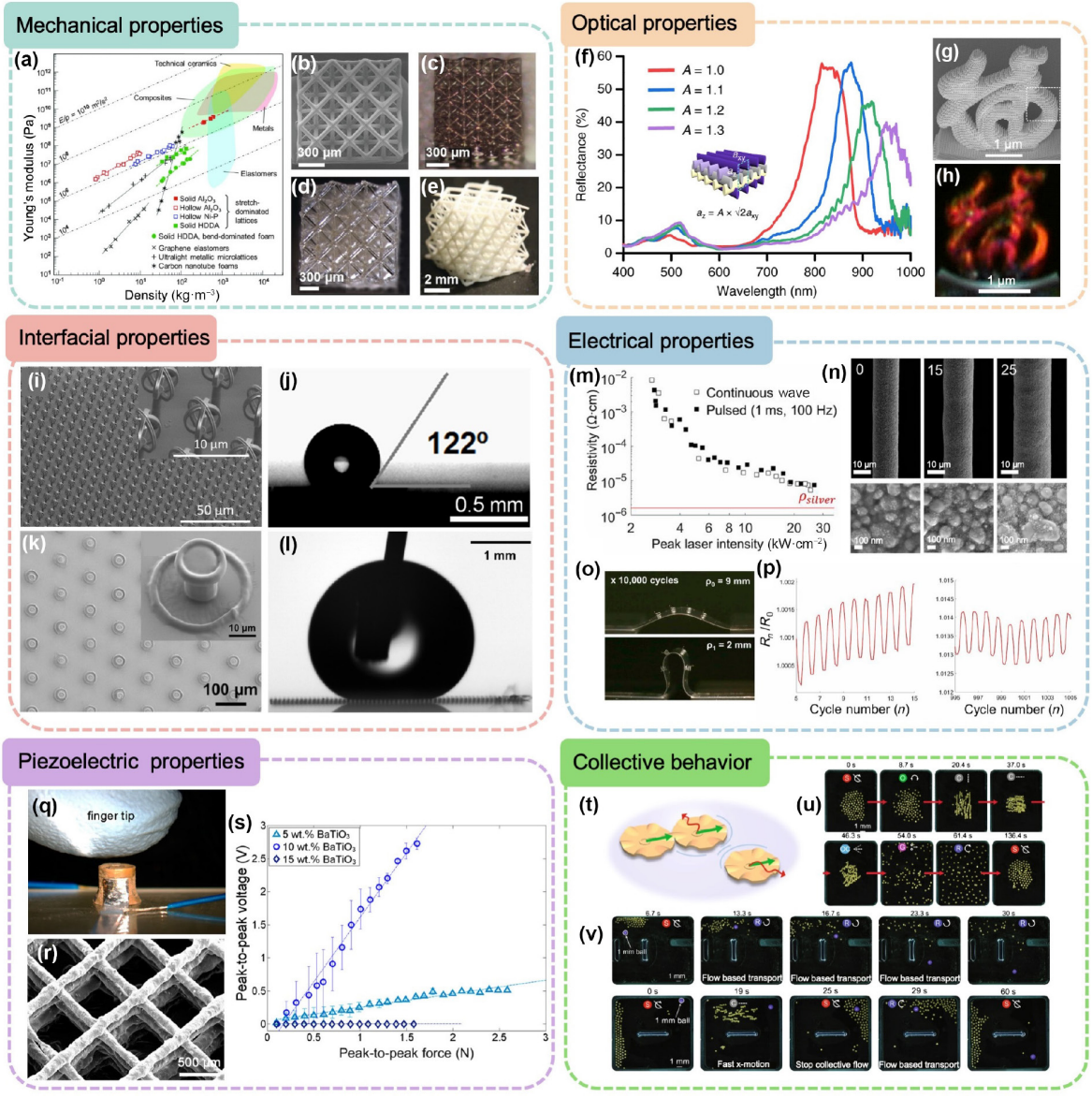

Figure 5 Micro-/nano-scale specific properties enabled by μnAM. (a) Comparison of mechanical properties of the lattice architectures. (b) Polymer lattice. (c) Ni–P lattice. (d) Hollow Al_2O_3 lattice. (e) Solid Al_2O_3 lattice. (f) Reflectance spectra of μnAM photonic crystals. Reproduced with permission with Ref. [60], © American Association for the Advancement of Science 2014. (g) Microstructure of a photonic crystal stack. (h) Photonic microstructure exhibiting structural color. Reproduced with permission with Ref. [113], © Liu, Y. J. et al. 2019. (i) Biomimetic microarray. (j) Static contact angle of the biomimetic surface. Reproduced with permission with Ref. [117], © American Chemical Society 2015. (k) Microarray fabricated by μnAM. (l) Static contact angle demonstrating superhydrophobicity. Reproduced with permission with Ref. [118], © Bunea, A. I. et al. 2023. (m) Electrical resistance as a function of processing or geometric parameters. (n) High-resolution conductive microstructure. (o) Microstructure subjected to cyclic mechanical testing. (p) Electrical resistance after cyclic testing. Reproduced with permission with Ref. [122], © Skylar-Scott, M. A. et al. 2016. (q) Piezoelectric device. (r) Piezoelectric microstructure. (s) Pressure–voltage response. Reproduced with permission with Ref. [126], © American Chemical Society 2017. (t) Schematic of microrobot design. (u) Collective behaviors under magnetic actuation. (v) Cargo transport. Reproduced with permission with Ref. [130], © Gardi, G. et al. 2022.

even deep-subwavelength scales, the printed architectures support complex light-matter interactions, including Bragg scattering, Mie resonances, and guided-mode coupling, which can be engineered through geometry rather than composition alone [110]. This enables precise control over reflection, transmission, and dispersion, giving rise to structural coloration, angle-dependent iridescence, and custom-designed photonic band structures. By leveraging multi-material μnAM, high-index dielectrics, plasmonic metals, and low-loss polymers can be combined within a single architecture, further expanding the design space for waveguides, filters, metasurfaces, and reconfigurable optical elements [111].

Fully 3D photonic crystals demand stringent dimensional control, making practical implementation challenging. Direct printing typically requires features sizes near 100 nm and lattice periodicities around 300 nm [112], pushing even state-of-the-art 2PP systems to their limits. Indirect approaches can bridge this gap. For instance, Liu et al. [113] printed polymer scaffolds by 2PP and then isotropically shrank them to achieve ≈ 280 nm features, comparable to the substructures found in butterfly wing scales, yielding vivid structural colors (Figs. 5(g) and 5(h)). The corresponding reflection spectra for varying hatch distances are shown in Fig. 5(f). Such μnAM-derived photonic crystals enable tunable optical responses for 3D microdisplays, anti-counterfeiting, and compact photonic components.

4.3 Interfacial properties

Conventional surface engineering relies on planar lithography to pattern large-area arrays [114]. μnAM surpasses this limitation by directly writing 3D microtextures that govern wetting, adhesion, and drag at will. By tailoring feature shape, spacing, and hierarchy at micro-/nanoscale, μnAM surfaces can access Cassie–Baxter, Wenzel, or hybrid wetting states on demand, enabling superhydrophobic, superhydrophilic, or anisotropic liquid transport behaviors [115]. Similarly, controlled asperity geometry and multi-material patterning allow switching between strong, gecko-inspired adhesion and low-adhesion release, while carefully designed riblets or porous textures can reduce viscous drag and manipulate boundary layers in fluid flow [116]. These capabilities transform interfaces from passive boundaries into actively engineered, function-bearing surfaces.

Tricinci et al. [117] used 2PP to fabricate artificial hair arrays inspired by *Salvinia molesta* leaves (Fig. 5(i)). The structures exhibited a static contact angle of 122° (Fig. 5(j)) and retained trapped air, indicating robust hydrophobicity. Bunea et al. [118] directly wrote polydimethylsiloxane (PDMS) microarrays using 2PP (Fig. 5(k)) and achieved superhydrophobic Cassie–Baxter states with maximum static contact angles near 158° (Fig. 5(l)). μnAM thus enables coating-free, durable water repellency and customizable interface properties for self-cleaning layers, microfluidics, and biomimetic surfaces.

4.4 Electrical properties

Conductive microstructures produced by μnAM combine complex geometry with high conductivity [119], allowing free-form 3D interconnects that are impractical with planar processes. By routing conductors through the volume rather than along a plane, μnAM enables compact, low-inductance wiring, vertical vias, and conformal electrodes that wrap around or penetrate 3D architectures. At the micro-/nanoscale, carefully designed cross-sections and pathway topologies can minimize resistive losses, control current density hotspots, and integrate sensing or heating elements directly into structural components [120]. When paired with multi-material capabilities, insulating, semiconducting, and metallic phases can be co-patterned within a single print, laying the groundwork for fully 3D integrated circuits, stretchable electronics, and embedded electrodes for electrochemical or biointerfacing applications [121].

Skylar-Scott et al. [122] fabricated Ag conductors via DIW with *in situ* laser-induced sintering and annealing. By tuning laser parameters, they achieved a minimum resistivity of 5.4×10^{-6} Ω·cm, approaching bulk silver (Fig. 5(m)), while maintaining high geometric fidelity (Fig. 5(n)). Cyclic compression tests showed stable conductivity after 1000 cycles (Figs. 5(o) and 5(p)). Such microstructured conductors are promising for flexible electronics, 3D antennas, and novel interconnect architectures.

4.5 Piezoelectric properties

Piezoelectric materials convert mechanical vibrations into electrical signals and are central to miniature energy harvesters and sensors. μnAM enhances piezoelectric performance by tailoring composition, crystal fraction, and microarchitecture during printing [123]. By defining the orientation and connectivity of piezoelectric phases within lightweight lattices or composite matrices, μnAM can concentrate strain in active regions, optimize poling pathways, and decouple stiffness from electromechanical coupling [124]. These design freedoms enable compact piezoelectric devices with higher sensitivity, improved energy conversion efficiency, and customized mode shapes for applications ranging from structural health monitoring to self-powered microsystems [125].

Bodkhe et al. [126] used DIW to incorporate $BaTiO_3$ NPs into polyvinylidene fluoride (PVDF), aided by solvent engineering, creating miniaturized piezoelectric elements (Fig. 5(q)) with fine feature control (Fig. 5(r)). With 10 wt.% $BaTiO_3$, the device produced ≈ 2.5 V under a 1.5 N load (Fig. 5(s)) and exhibited a piezoelectric coefficient of ≈ 18 pC/N, comparable to stretched and poled PVDF films. Spatially patterned 3D piezoelectric networks can thereby improve electromechanical coupling and directional strain sensitivity in compact systems.

4.6 Collective behavior of micro-/nanorobots

μnAM facilitates large populations of nearly identical microrobots with complex, repeatable features, enabling studies of collective dynamics reminiscent of living systems [127]. By precisely encoding body geometry, mass distribution, and local responsiveness (e.g., to light, magnetic fields, or chemical gradients) into each unit, μnAM allows robots to share the same "hardware genome" while exhibiting rich emergent behaviors at the swarm level. Micro-/nanorobots can be designed to interact through hydrodynamic, capillary, magnetic, or contact forces, giving rise to self-organization, clustering, phase separation, and flocking-like motions that are difficult to realize with macroscale platforms [128]. Multi-material architectures further allow heterogeneous task allocation within a swarm, combining cargo carriers, leaders, and environmental sensors, thus opening pathways toward programmable, physically intelligent collectives for targeted delivery, environmental remediation, and adaptive micromanipulation [129].

Gardi et al. [130] fabricated ≈ 300 μm microrobots by 2PP (Fig. 5(t)). When actuated by a dynamic magnetic field at an air-water interface, the swarms displayed coordinated rotation, chain

formation, aggregation, and gas-like dispersion (Fig. 5(u)). By tuning the field parameters, the swarm transported a 1 mm ball and navigated obstacles (Fig. 5(v)). These results show how μnAM-built microrobots can function as reconfigurable, programmable matter. Future applications may include targeted operations in biomedical and other complex environments.

5 Advanced applications

5.1 Optical devices

At micro-/nanoscales, optical phenomena become particularly prominent, as discussed in Section 4.2. In optical micro-/nano devices, μnAM is therefore not only about pushing printing resolution; instead, it leverages precisely defined 3D geometries and interfaces so that the structures themselves perform the optical function. By tailoring lattice periodicity, surface relief, and refractive-index distributions in three dimensions, μnAM-enabled architectures can realize high numerical aperture, chromatic aberration correction, structural color, and other advanced optical responses that are difficult to achieve with conventional planar fabrication.

Firstly, μnAM enables the miniaturization of traditional, large-volume optical components to micrometer scales, expanding the use of highly demanding compact optical devices. Richards et al. [131] employed 2PP to print hybrid achromatic microlens arrays within porous substrates (Fig. 6(a)). By exploiting intra-band dispersion compensation among the constituent elements, these devices maintain accuracy and performance in extremely small form factors. Marini et al. [132] fabricated microlens arrays that provide high-contrast, high-spatial-resolution imaging at very short working distances (Fig. 6(b)). The authors noted that such miniaturized lenses can be implanted for *in vivo* tissue imaging, substantially reducing patient discomfort.

Secondly, μnAM also enables complex optical structures that are infeasible with conventional fabrication. Webber et al. [133] directly wrote continuous refractive-index distributions and free-form surface geometries within a resin matrix, producing microlenses with negligible layer striations and low surface roughness. They demonstrated a double-sided biconvex microlens array with complex geometry that can be overprinted onto an optical fiber (Fig. 6(c)). In parallel, Hsu et al. [134] used 2PP to create flower-like liquid-crystal elastomer architectures that guide liquid-crystal alignment into intricate patterns, yielding optical responses difficult to achieve with traditional methods (Fig. 6(d)).

In addition, structural color produced by μnAM offers a promising alternative to chemical dyes. Kim et al. [135] directly wrote complex structural-color patterns on planar substrates and then applied isotropic shrinkage to reduce the lattice constant, achieving intense Bragg reflection while preserving high resolution (Fig. 6(e)). Demirörs et al. [136] reported 3D printing of photopolymerizable photonic colloidal glasses, whose short-range order and long-range disorder yield angle-insensitive, isotropic structural colors that extend from planar films to arbitrary 3D geometries (Fig. 6(f)). Overall, μnAM provides a high degree of structural programmability in optics and is advancing toward increasingly fine and sophisticated applications.

5.2 Micro-/nano sensors

Microsystems are becoming indispensable in modern life. To operate reliably in complex environments, however, they require precise, continuous, and multidimensional sensing. Owing to the

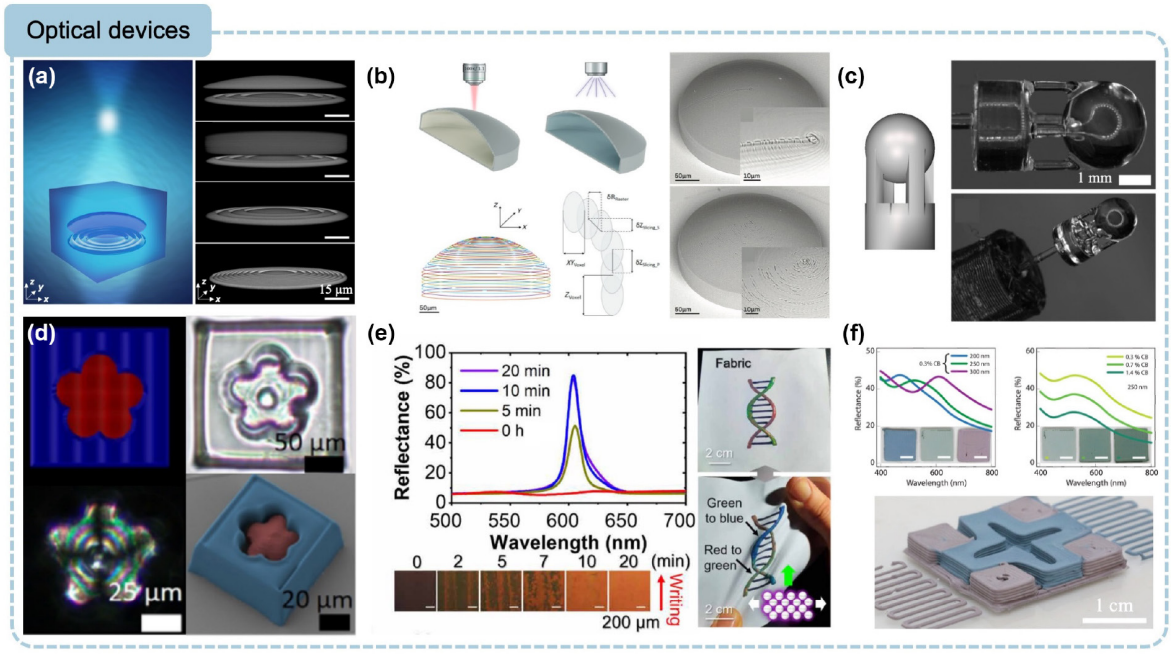

Figure 6 Applications in optical devices. (a) Diagram of compact hybrid achromatic microlenses. Reproduced with permission with Ref. [131], © Richards, C. A. et al. 2023. (b) Schematic diagram and scanning electron microscope images of the micro-lens manufacturing process for precise curvature. Reproduced with permission with Ref. [132], © Marini, M. et al. 2023. (c) Overprinting complex structured ball lenses onto an optical fiber. Reproduced with permission with Ref. [133], © Optica Publishing Group 2024. (d) Liquid crystal structure (red) printed in PDMS micro scaffold (blue) and optical effect images. Reproduced with permission with Ref. [134], © Hsu, L. Y. et al. 2024. (e) Temporal evolutions of the reflectance spectrum and optical texture for a face drawn using an ethoxylate acrylate ink, and double helix patterns with different colors. Reproduced with permission with Ref. [135], © Kim, J. B. et al. 2021. (f) Reflectance spectra of 3D printed and heat-treated specimens prepared using different silica particle sizes and carbon black (CB), and 3D structures with different colors. Reproduced with permission with Ref. [136], © Demirörs, A. F. et al. 2022.

programmable architectures and material distributions enabled by μnAM, miniature devices can be engineered to detect pressure, temperature, gases, bodily fluids, and biochemical signals via microneedle or implanted interfaces, allowing tightly integrated sensing at the micro-/nano-scale dimensions.

μnAM supports a broad range of physical-signal sensors. Xu et al. [137] used electric-field-assisted FDM to create grid structures with strain-concentrating geometries, thereby tuning piezoelectric and piezoresistive responses and markedly improving sensitivity over conventional cast designs (Fig. 7(a)). Xu et al. [138] patterned liquid-metal strain sensors by AJP, achieving minimum line widths of 12 μm on multiple substrates (Fig. 7(b)) and ultralow strain-detection limits suitable for comprehensive motion monitoring. Roy et al. [139] employed high-precision DIW to integrate conductive networks with soft encapsulation layers, yielding skin-conformal devices that maintain sensing stability while providing robust bio-adhesion and mechanical compliance, with tunable electronic and thermal biosensing capabilities (Fig. 7(c)).

Beyond physical signals, μnAM also enables chemical and biochemical sensing. Ahmadipour et al. [140] used EJP printing to deposit an ion-liquid-functionalized $Cu_3(HHTP)_2$ metal organic framework (MOF) onto electrospun PLA for NO-gas detection (Fig. 7(d)), achieving nearly sixfold higher response accuracy than conventional MOF sensors. Chen et al. [141] used DIW to fabricate microchannels and conductive elements for a sweat-analysis patch that monitors sweat rate, glucose, lactate, and uric acid *in situ* during exercise (Fig. 7(e)). Song et al. [142] realized fully 3D-printed systems via semi-solid extrusion, co-fabricating electrochemical and physiological sensors, microfluidics, and miniature supercapacitors, thereby enabling electrochemical sweat biosensing (glucose, alcohol, pH) alongside biophysical sensing (temperature, pulse) within a single device (Fig. 7(f)). Dadras-Toussi et al. [143] used multiphoton direct writing, similar to 2PP, to print organic-semiconductor microcircuits (Fig. 7(g)); with integrated glucose oxidase, the resulting sensors achieved nearly tenfold higher glucose sensitivity compared with prior designs.

However, above patch-type sensors typically probe only superficial biomarkers. μnAM-fabricated microneedles that traverse the skin barrier help overcome this limitation. By precisely defining tip geometry and overall architecture, these devices enable minimally invasive penetration and localized, accurate detection

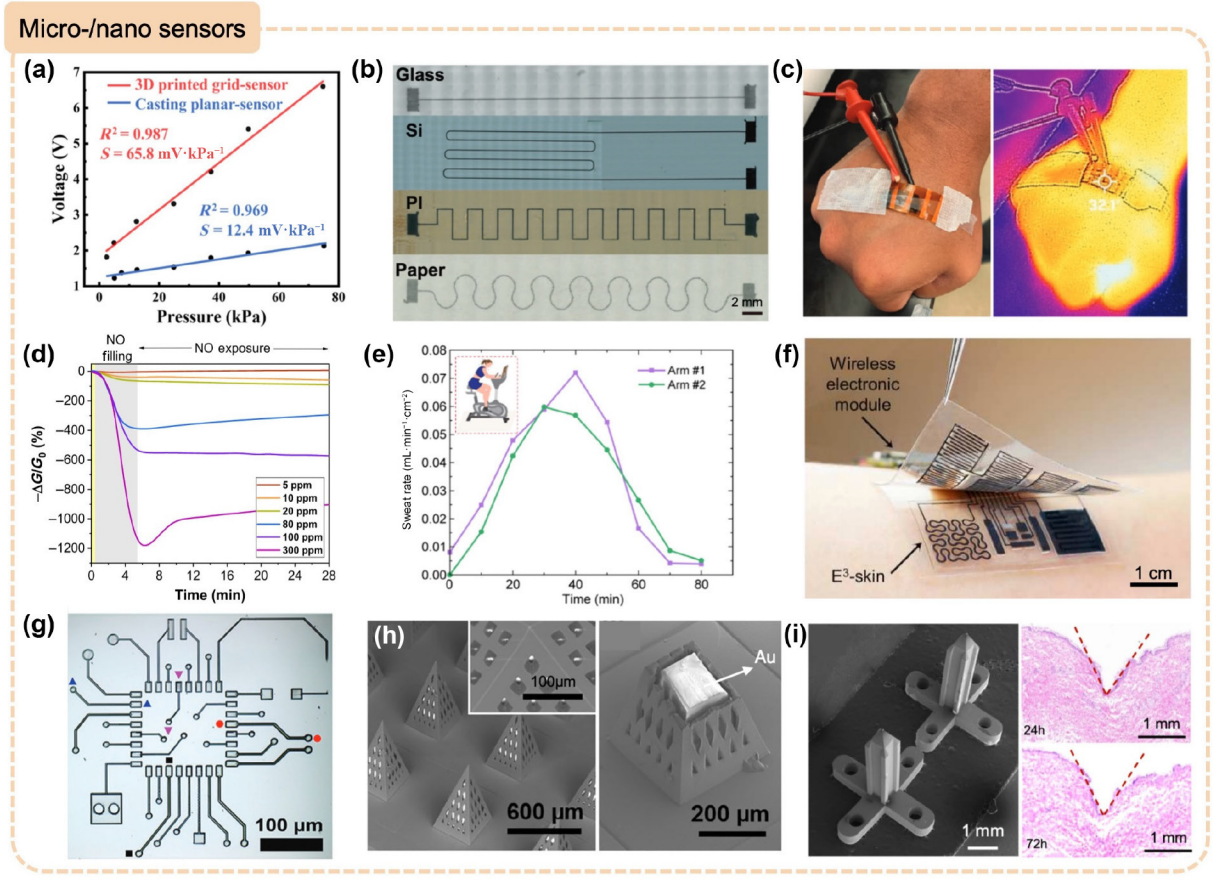

Figure 7 Applications in micro-/nano sensors. (a) Comparison of piezoelectric properties for 3D printed sensor and casting sensor. Reproduced with permission from Ref. [137], © American Chemical Society 2025. (b) AJP printing of various sensor patterns on different substrates. Reproduced with permission from Ref. [138], © Xu, B. Y. et al. 2025. (c) Real-time monitoring of body temperature using electronic skin as a flexible thermometer. Reproduced with permission from Ref. [139], © Roy, S. et al. 2024. (d) Chemiresistive response of EJP printed IL-functionalized $Cu_3(HHTP)_2$ MOF sensor to various NO gas concentrations. Reproduced with permission from Ref. [140], © Ahmadipour, M. et al. 2025. (e) *In situ* monitoring of the correlation between sweating rate and time in two positions of the left arm. Reproduced with permission from Ref. [141], © American Chemical Society 2024. (f) 3D-printed e³-skin worn on a human subject. Reproduced with permission from Ref. [142], © Song, Y. et al. 2023. (g) Optical microscopy image of a micro printed circuit board comprised of various electrical elements. Reproduced with permission from Ref. [143], © Wiley-VCH GmbH 2022. (h) SEM images of electrode arrays and cross-section (the shell is polymeric lattice, and inside is Au). Reproduced with permission from Ref. [145], © Wiley-VCH GmbH 2024. (i) SEM images of 3D printing microneedle and representative histology images of local skin after glucose/metformin sensor implantation for 24 and 72 h. Reproduced with permission from Ref. [146], © Dervisevic, M. et al. 2025.

[144]. Dervisevic et al. [145] used 2PP and soft lithography to print microneedle arrays with lightweight lattice shell and Au cores (Fig. 7(h)), providing sufficient mechanical strength for insertion while reducing pain perception. The functional layers embedded within the needle body enabled *in situ* sensing of glucose and insulin. In addition, Yang et al. [146] fabricated implantable structures with multi-column supports and anchoring features (Fig. 7(i)), achieving accurate monitoring of glucose and metformin in the body.

5.3 Micro-/nanorobots

Micro-/nanorobots can achieve directional motion, precise manipulation, and diverse task execution across varied environments through external field actuation [147]. μnAM integrates mechanical, optical, and interfacial effects into individual or collective robotic systems, enabling their extensive applications in complex scenarios such as precision medicine, tissue engineering, and environmental conservation.

By constructing complex 3D architectures with programmed asymmetry in shape, stiffness, and material distribution, μnAM allows micro-/nanorobots to exhibit tailored propulsion modes, steering capabilities, and task-specific responses under a given actuation field. For example, μnAM can print intricate structures such as helices for directionally propelled microrobots. Tottori et al. [148] used 3D direct laser writing to fabricate magnetic helical robots 4–60 μm in size, where helix geometry governed propulsion efficiency; they also demonstrated microgrippers for coordinated grasping, transport, and release (Fig. 8(a)). Mahkam et al. [149] fabricated microrobots actuated by ultrasonic fields, incorporating bubbles within microcavities and nozzle-like structures (Fig. 8(b)). These designs fully exploit μnAM's capability to build 3D cavity geometries.

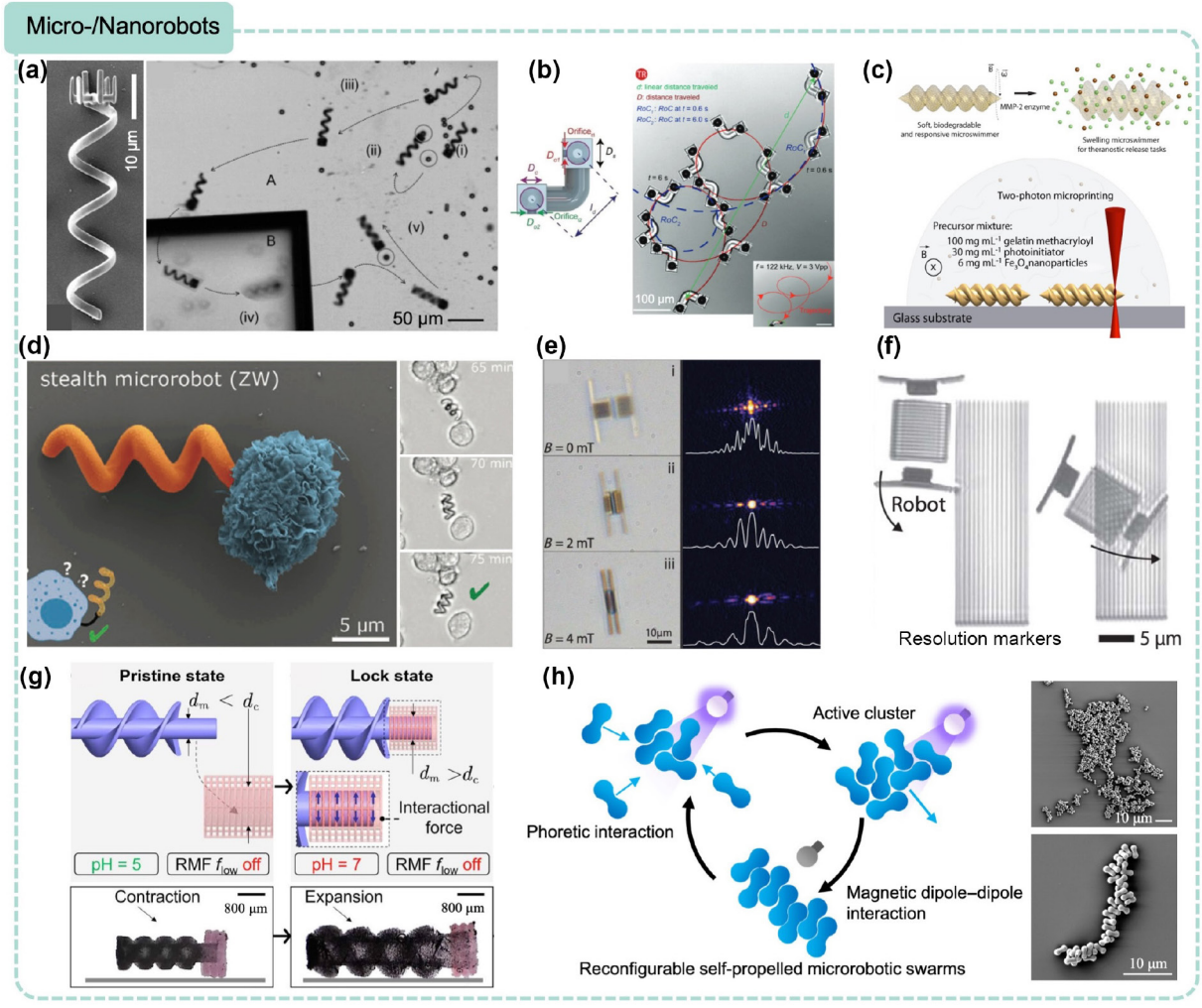

Figure 8 Applications in micro-/nanorobots. (a) Helical micromachine with a microholder; time-lapse image of the pick-and-place micromanipulation of a magnetic microparticle. Reproduced with permission from Ref. [148], © WILEY-VCH Verlag GmbH & Co. KGaA, Weinheim 2012. (b) Schematics of the bubble-driven microrobot and its sliding under the action of the sound wave. Reproduced with permission from Ref. [149], © Mahkam, N. et al. 2023. (c) Schematic diagram of the double-helix robots releasing drugs and the 2PP manufacturing process. Reproduced with permission from Ref. [150], © American Chemical Society 2019. (d) Schematic diagram of the interaction of the macrophage and the stealth microrobot, and optical microscopy images of the immune escape process. Reproduced with permission from Ref. [151], © Cabanach, P. et al. 2020. (e) Compression of the microrobot under different uniform magnetic field magnitudes and diffraction images. (f) Appearance of Moiré fringes as the robot walks over to 800-nm-wide resolution markers. Reproduced with permission from Ref. [152], © Smart, C. L. et al. 2024. (g) Schematic diagram of the assembly and disassembly process in different pH environments. Reproduced with permission from Ref. [153], © Su, L. et al. 2023. (h) Reconfigurable, reversible, and active self-assembly of robots under light stimulation, and SEM images of the collective behavior of the robots. Reproduced with permission from Ref. [154], © Urso, M. et al. 2023.

Multi-material fabrication further broadens micro-/nanorobots' capabilities by allowing control over biodegradability, mechanical compliance, and immune interactions. Ceylan et al. [150] printed helical robots via 2PP using a gelatin methacryloyl (GelMA) network loaded with iron-oxide NPs (Fig. 8(c)). These robots released drugs through localized hydrogel swelling and, owing to the introduction of target-specific cleavage sites, exhibited rapid degradability. Cabanach et al. [151] fabricated magnetic stealth microrobots by 2PP and achieved immune evasion through surface functionalization using fully zwitterionic photoresists during printing (Fig. 8(d)).

Beyond field-driven locomotion, μnAM enables intelligent self-assembly in response to external stimuli. Smart et al. [152] combined nanometer-thick mechanical films, programmable nanomagnets, and diffractive optical elements to build microrobots that reconfigure in millitesla magnetic fields (Fig. 8(e)) and operate at the visible-light diffraction limit, which makes them viable as tunable diffractive optics for beam control and focusing (Fig. 8(f)). Su et al. [153] printed pH-responsive magnetoactuator modules and biocompatible cell-scaffold modules that lock in acidic environments and unlock under neutral conditions (Fig. 8(g)); these systems support image-guided navigation, *in situ* cell release, and magnetic component recovery.

Collective behavior emerges naturally from such self-assembly. As discussed in Section 4.6, coordinated swarms can express functions that exceed a simple sum of single-robot actions. Urso et al. [154] demonstrated dual-mode regulation that couples light-driven autodiffusive swimming with magnetic dipole–dipole interactions, enabling reversible reconfiguration of microrobot swarms among chain-like, cluster-like, and ribbon-like states (Fig. 8(h)).

6 Summaries and outlook

μnAM is rapidly evolving from a set of niche techniques into a versatile platform for architecting matter in 3D across polymers, metals, ceramics, and their combinations. In this review, we have mapped the field from process fundamentals (transformation-assisted, powder-bed, extrusion, jetting, and photopolymerization) to material strategies (template- and precursor-based routes, NP/NC assembly) and scale-specific properties (mechanical, optical, interfacial, electrical, piezoelectric, properties, and collective behaviors), and further to applications in optical devices, sensors, and micro-/nanorobots. A key emerging theme is the transition from "printable resins" to "any-material voxels", where μnAM provides the scaffold and spatial precision, and subsequent chemical, thermal, or field-driven transformations define the final functional composition.

Despite substantial progress has been made, several challenges must be addressed before μnAM can mature into an industry-ready manufacturing paradigm. Long writing times and cumulative 3D stitching can introduce dimensional errors, where even small inaccuracies can compound into significant deviations. In multi-material fabrication, persistent issues include cross-contamination, inter-material registration, interfacial defects, and residual stress. Moreover, design and modelling capabilities lag behind fabrication: fully exploiting micro-/nano-scale effects will require multiphysics and multiscale design frameworks, robust inverse-design tools, and open datasets tailored to μnAM, rather than simple downscaling of macroscale concepts.

Looking ahead, progress on multiple fronts can collectively mitigate these obstacles. Hybrid and parallel workflows that integrate μnAM with photolithography, self-assembly, and conventional AM can relax constraints on resolution and throughput. Beyond layerwise fabrication, volumetric additive manufacturing (VAM) offers a potential route to significantly higher throughput by forming 3D structures through volumetric exposure, although micro-/nano-scale implementation is still limited by optical scattering/absorption, and voxel cross-talk. Meanwhile, *in situ* multi-material synthesis is emerging as another frontier, where reactive precursors are locally converted during or immediately after writing to directly encode composition and interfaces. However, its practical adoption remains constrained by precursor/material compatibility and reliable *in situ* methodology. In parallel, AI- and data-driven design frameworks can close the gap between fabrication and modelling: By learning process–structure–property relationships from μnAM-specific datasets, generative and inverse-design algorithms can propose architected geometries and multi-material compositions that optimally exploit micro-/nano-scale effects under given constraints. Coupled with *in situ* metrology and closed-loop process control, such AI-enabled pipelines could autonomously refine voxel-level composition, topology, and printing parameters, accelerating the discovery of μnAM architectures beyond what is accessible by manual, trial-and-error design. At the application level, tighter coupling among device design, reliability testing, and standards specific to target use cases will accelerate translation in optical devices, sensors, and micro-/nanorobotics.

Overall, μnAM is poised to remain a central driver at the intersection of micro-/nano-engineering, advanced manufacturing, and functional materials [155]. With continued developments in processes, materials, and AI-enhanced design methodologies, we anticipate broad application prospects and significant growth potential for multi-material μnAM in the coming decade.

Data availability

Not applicable.

Acknowledgements

M. Z. acknowledges support and funding from the National University of Singapore Presidential Young Professorship Start Up Grant (No. A-0010080-00-00).

Declaration of competing interest

All the contributing authors report no conflict of interests in this work.

Author contribution statement

H. H. X.: Data curation, writing manuscript. Z. H. X.: Data curation, writing manuscript. H. J. L.: Revising manuscript, validation. M. C. Z.: Project administration, funding acquisition, revising manuscript.

Use of AI statement

None.

References

[1] Beaman, J. J.; Bourell, D. L.; Seepersad, C. C.; Kovar, D. Additive

manufacturing review: Early past to current practice. *J. Manuf. Sci. Eng.* **2020**, *142*, 110812.
[2] Ngo, T. D.; Kashani, A.; Imbalzano, G.; Nguyen, K. T. Q.; Hui, D. Additive manufacturing (3D printing): A review of materials, methods, applications and challenges. *Compos. Part B: Eng.* **2018**, *143*, 172–196.
[3] Guo, N. N.; Leu, M. C. Additive manufacturing: Technology, applications and research needs. *Front. Mech. Eng.* **2013**, *8*, 215–243.
[4] Kelly, B. E.; Bhattacharya, I.; Heidari, H.; Shusteff, M.; Spadaccini, C. M.; Taylor, H. K. Volumetric additive manufacturing via tomographic reconstruction. *Science* **2019**, *363*, 1075–1079.
[5] Bernal, P. N.; Florczak, S.; Inacker, S.; Kuang, X.; Madrid-Wolff, J.; Regehly, M.; Hecht, S.; Zhang, Y. S.; Moser, C.; Levato, R. The road ahead in materials and technologies for volumetric 3D printing. *Nat. Rev. Mater.* **2025**, *10*, 826–841.
[6] Ikumapayi, O. M.; Akinlabi, E. T.; Adeoye, A. O. M.; Fatoba, S. O. Microfabrication and nanotechnology in manufacturing system - An overview. *Mater. Today: Proc.* **2021**, *44*, 1154–1162.
[7] Quake, S. R.; Scherer, A. From micro- to nanofabrication with soft materials. *Science* **2000**, *290*, 1536–1540.
[8] Liu, S. F.; Hou, Z. W.; Lin, L. H.; Li, Z. C.; Sun, H. B. 3D laser nanoprinting of functional materials. *Adv. Funct. Mater.* **2023**, *33*, 2211280.
[9] Wu, B. Q.; Kumar, A. Extreme ultraviolet lithography and three dimensional integrated circuit—A review. *Appl. Phys. Revi.* **2014**, *1*, 011104.
[10] Bratton, D.; Yang, D.; Dai, J. Y.; Ober, C. K. Recent progress in high resolution lithography. *Polym. Adv. Technol.* **2006**, *17*, 94–103.
[11] Kumar, R.; Kumar, M.; Chohan, J. S. Material-specific properties and applications of additive manufacturing techniques: A comprehensive review. *Bull. Mater. Sci.* **2021**, *44*, 181.
[12] Su, R. Y.; Chen, J. Y.; Zhang, X. Q.; Wang, W. Q.; Li, Y.; He, R. J.; Fang, D. N. 3D-printed micro/nano-scaled mechanical metamaterials: Fundamentals, technologies, progress, applications, and challenges. *Small* **2023**, *19*, e2206391.
[13] Zhang, Y. H.; Zhang, F.; Yan, Z.; Ma, Q.; Li, X. L.; Huang, Y. G.; Rogers, J. A. Printing, folding and assembly methods for forming 3D mesostructures in advanced materials. *Nat. Rev. Mater.* **2017**, *2*, 17019.
[14] Schmidt, O. G.; Eberl, K. Thin solid films roll up into nanotubes. *Nature* **2001**, *410*, 168–168.
[15] Ahn, J.; Ha, J. H.; Jeong, Y.; Jung, Y.; Choi, J.; Gu, J. M.; Hwang, S. H.; Kang, M. G.; Ko, J.; Cho, S. et al. Nanoscale three-dimensional fabrication based on mechanically guided assembly. *Nat. Commun.* **2023**, *14*, 833.
[16] Ning, X.; Wang, X. J.; Zhang, Y.; Yu, X. G.; Choi, D.; Zheng, N.; Kim, D. S.; Huang, Y. G.; Zhang, Y. H.; Rogers, J. A. Assembly of advanced materials into 3D functional structures by methods inspired by origami and kirigami: A review. *Adv. Mater. Interfaces* **2018**, *5*, 1800284.
[17] Zhang, M. C.; Shahsavan, H.; Guo, Y. B.; Pena-Francesch, A.; Zhang, Y. Y.; Sitti, M. Liquid-crystal-elastomer-actuated reconfigurable microscale kirigami metastructures. *Adv. Mater.* **2021**, *33*, 2008605.
[18] Bo, R. H.; Xu, S. W.; Yang, Y. Z.; Zhang, Y. H. Mechanically-guided 3D assembly for architected flexible electronics. *Chem. Rev.* **2023**, *123*, 11137–11189.
[19] Cheng, X.; Shen, Z. M.; Zhang, Y. H. Bioinspired 3D flexible devices and functional systems. *Nat. Sci. Rev.* **2024**, *11*, nwad314.
[20] Singh, R.; Gupta, A.; Tripathi, O.; Srivastava, S.; Singh, B.; Awasthi, A.; Rajput, S. K.; Sonia, P.; Singhal, P.; Saxena, K. K. Powder bed fusion process in additive manufacturing: An overview. *Mater. Today: Proc.* **2020**, *26*, 3058–3070.
[21] Xiang, H. H.; Dang, M. Z.; Li, J. K.; Zhang, Z. W.; Gao, H. R.; Cai, C.; Wei, Q. S. Achieving dual-phase structured Cu-Al-Mn-Si alloy with prominent shape memory properties via laser powder bed fusion. *Addit. Manuf.* **2024**, *95*, 104521.
[22] Sow, M. C.; De Terris, T.; Castelnau, O.; Hamouche, Z.; Coste, F.; Fabbro, R.; Peyre, P. Influence of beam diameter on laser powder bed fusion (L-PBF) process. *Addit. Manuf.* **2020**, *36*, 101532.
[23] Fischer, J.; Kniepkamp, M.; Abele, E. Micro laser melting: Analyses of current potentials and restrictions for the additive manufacturing of micro structures. In *Twenty- Fifth Annual International Solid Freeform Fabrication*, Austin, USA, 2014, pp 22–35.
[24] Hu, Z. X.; Chen, H.; Yang, Z. S.; Yan, W. T. Critical role of electrostatic forces in powder spreading in micro laser powder bed fusion. *Addit. Manuf.* **2025**, *109*, 104848.
[25] Fu, J.; Hu, Z. H.; Song, X.; Zhai, W.; Long, Y.; Li, H.; Fu, M. W. Micro selective laser melting of NiTi shape memory alloy: Defects, microstructures and thermal/mechanical properties. *Opt. Laser Technol.* **2020**, *131*, 106374.
[26] Hu, Z. H.; Nagarajan, B.; Song, X.; Huang, R.; Zhai, W.; Wei, J. Formation of SS316L single tracks in micro selective laser melting: Surface, geometry, and defects. *Adv. Mater. Sci. Eng.* **2019**, *2019*, 9451406.
[27] Nagarajan, B.; Hu, Z. H.; Song, X.; Zhai, W.; Wei, J. Development of micro selective laser melting: The state of the art and future perspectives. *Engineering* **2019**, *5*, 702–720.
[28] Saadi, M. A. S. R.; Maguire, A.; Pottackal, N. T.; Thakur, M. S. H.; Ikram, M. M.; Hart, A. J.; Ajayan, P. M.; Rahman, M. M. Direct ink writing: A 3D printing technology for diverse materials. *Adv. Mater.* **2022**, *34*, 2108855.
[29] Zhang, M. C.; Zhao, M. Y.; Jian, M. Q.; Wang, C. Y.; Yu, A. F.; Yin, Z.; Liang, X. P.; Wang, H. M.; Xia, K. L.; Liang, X. et al. Printable smart pattern for multifunctional energy-management E-textile. *Matter* **2019**, *1*, 168–179.
[30] Li, L.; Meng, J.; Bao, X. R.; Huang, Y. P.; Yan, X. P.; Qian, H. L.; Zhang, C.; Liu, T. X. Direct-ink-write 3D printing of programmable micro-supercapacitors from MXene-regulating conducting polymer inks. *Adv. Energy Mater.* **2023**, *13*, 2203683.
[31] Zheng, Q. Y.; Xie, B.; Xu, Z. L.; Wu, H. A systematic printability study of direct ink writing towards high-resolution rapid manufacturing. *Int. J. Extrem. Manuf.* **2023**, *5*, 035002.
[32] Estelle, K. T.; Gozen, B. A. Complex ink flow mechanisms in micro-direct-ink-writing and their implications on flow rate control. *Addit. Manuf.* **2022**, *59*, 103183.
[33] Rodríguez-Panes, A.; Claver, J.; Camacho, A. M. The influence of manufacturing parameters on the mechanical behaviour of PLA and ABS pieces manufactured by FDM: A comparative analysis. *Materials* **2018**, *11*, 1333.
[34] Cano-Vicent, A.; Tambuwala, M. M.; Hassan, S. S.; Barh, D.; Aljabali, A. A. A.; Birkett, M.; Arjunan, A.; Serrano-Aroca, Á. Fused deposition modelling: Current status, methodology, applications and future prospects. *Addit. Manuf.* **2021**, *47*, 102378.
[35] Romanov, V.; Samuel, R.; Chaharlang, M.; Jafek, A. R.; Frost, A.; Gale, B. K. FDM 3D printing of high-pressure, heat-resistant, transparent microfluidic devices. *Anal. Chem.* **2018**, *90*, 10450–10456.
[36] Quero, R. F.; Domingos Da Silveira, G.; Fracassi Da Silva, J. A.; De Jesus, D. P. Understanding and improving FDM 3D printing to fabricate high-resolution and optically transparent microfluidic devices. *Lab Chip* **2021**, *21*, 3715–3729.
[37] Bol, R. J. M.; Šavija, B. Micromechanical models for FDM 3D-printed polymers: A review. *Polymers* **2023**, *15*, 4497.
[38] Secor, E. B. Principles of aerosol jet printing. *Flex. Print. Electron.* **2018**, *3*, 035002.
[39] Hu, C. S.; Jahan, S.; Yuan, B.; Panat, R. 3D-AJP: Fabrication of

advanced microarchitected multimaterial ceramic structures via binder-free and auxiliary-free aerosol jet 3D nanoprinting. *Adv. Sci.* **2025**, *12*, 2405334.

[40] Liu, L.; Xu, Z. H.; Molina Vargas, A. M.; Dollery, S. J.; Schrlau, M. G.; Cormier, D.; O'Connell, M. R.; Tobin, G. J.; Du, K. Aerosol jet printing-enabled dual-function electrochemical and colorimetric biosensor for SARS-CoV-2 detection. *Anal. Chem.* **2023**, *95*, 11997–12005.

[41] Turan, N.; Saeidi-Javash, M.; Chen, J. H.; Zeng, M. X.; Zhang, Y. L.; Go, D. B. Atmospheric pressure and ambient temperature plasma jet sintering of aerosol jet printed silver nanoparticles. *ACS Appl. Mater. Interfaces* **2021**, *13*, 47244–47251.

[42] Wilkinson, N. J.; Smith, M. A. A.; Kay, R. W.; Harris, R. A. A review of aerosol jet printing—a non-traditional hybrid process for micro-manufacturing. *Int. J. Adv. Manuf. Technol.* **2019**, *105*, 4599–4619.

[43] Salary, R. R.; Lombardi III, J. P.; Weerawarne, D. L.; Rao, P. K.; Poliks, M. D. A state-of-the-art review on aerosol jet printing (AJP) additive manufacturing process. In *ASME 2019 14th International Manufacturing Science and Engineering Conference*, Erie, USA, 2019.

[44] Park, J. U.; Hardy, M.; Kang, S. J.; Barton, K.; Adair, K.; Mukhopadhyay, D. K.; Lee, C. Y.; Strano, M. S.; Alleyne, A. G.; Georgiadis, J. G. et al. High-resolution electrohydrodynamic jet printing. *Nat. Mater.* **2007**, *6*, 782–789.

[45] Yin, Z. P.; Wang, D. Z.; Guo, Y. L.; Zhao, Z. Y.; Li, L. Q.; Chen, W.; Duan, Y. Q. Electrohydrodynamic printing for high resolution patterning of flexible electronics toward industrial applications. *InfoMat* **2024**, *6*, e12505.

[46] Onses, M. S.; Sutanto, E.; Ferreira, P. M.; Alleyne, A. G.; Rogers, J. A. Mechanisms, capabilities, and applications of high-resolution electrohydrodynamic jet printing. *Small* **2015**, *11*, 4237–4266.

[47] Reizabal, A.; Tandon, B.; Lanceros-Méndez, S.; Dalton, P. D. Electrohydrodynamic 3D printing of aqueous solutions. *Small* **2023**, *19*, 2205255.

[48] Zhou, H. H.; Song, Y. L. Fabrication of electronics by electrohydrodynamic jet printing. *Adv. Electron. Mater.* **2022**, *8*, 2200728.

[49] Khan, A.; Rahman, K.; Ali, S.; Khan, S.; Wang, B.; Bermak, A. Fabrication of circuits by multi-nozzle electrohydrodynamic inkjet printing for soft wearable electronics. *J. Mater. Res.* **2021**, *36*, 3568–3578.

[50] Zhong, Y.; Yu, H. B.; Zhou, P. L.; Wen, Y. D.; Zhao, W. X.; Zou, W. H.; Luo, H.; Wang, Y. C.; Liu, L. Q. *In situ* electrohydrodynamic jet printing-based fabrication of tunable microlens arrays. *ACS Appl. Mater. Interfaces* **2021**, *13*, 39550–39560.

[51] Jacobsen, A. J.; Barvosa-Carter, W.; Nutt, S. Micro-scale truss structures with three-fold and six-fold symmetry formed from self-propagating polymer waveguides. *Acta Mater.* **2008**, *56*, 2540–2548.

[52] Jacobsen, A. J.; Barvosa-Carter, W.; Nutt, S. Shear behavior of polymer micro-scale truss structures formed from self-propagating polymer waveguides. *Acta Mater.* **2008**, *56*, 1209–1218.

[53] Mao, Y. J.; Xu, L.; Lin, H.; Li, J.; Yan, D. X.; Zhong, G. J.; Li, Z. M. Effective electromagnetic interference shielding properties of micro-truss structured CNT/Epoxy composites fabricated based on visible light processing. *Compos. Sci. Technol.* **2022**, *221*, 109296.

[54] Jacobsen, A. J.; Barvosa-Carter, W.; Nutt, S. Micro-scale truss structures formed from self-propagating photopolymer waveguides. *Adv. Mater.* **2007**, *19*, 3892–3896.

[55] Schaedler, T. A.; Jacobsen, A. J.; Torrents, A.; Sorensen, A. E.; Lian, J.; Greer, J. R.; Valdevit, L.; Carter, W. B. Ultralight metallic microlattices. *Science* **2011**, *334*, 962–965.

[56] Kolodziejska, J. A.; Roper, C. S.; Yang, S. S.; Carter, W. B.; Jacobsen, A. J. Research update: Enabling ultra-thin lightweight structures: Microsandwich structures with microlattice cores. *APL Mater.* **2015**, *3*, 050701.

[57] Huang, J. G.; Qin, Q.; Wang, J. A review of stereolithography: Processes and systems. *Processes* **2020**, *8*, 1138.

[58] Emami, M. M.; Barazandeh, F.; Yaghmaie, F. Scanning-projection based stereolithography: Method and structure. *Sensors Actuat. A: Phys.* **2014**, *218*, 116–124.

[59] Zheng, X. Y.; Smith, W.; Jackson, J.; Moran, B.; Cui, H. C.; Chen, D.; Ye, J. C.; Fang, N.; Rodriguez, N.; Weisgraber, T. et al. Multiscale metallic metamaterials. *Nat. Mater.* **2016**, *15*, 1100–1106.

[60] Zheng, X. Y.; Lee, H.; Weisgraber, T. H.; Shusteff, M.; DeOtte, J.; Duoss, E. B.; Kuntz, J. D.; Biener, M. M.; Ge, Q.; Jackson, J. A. et al. Ultralight, ultrastiff mechanical metamaterials. *Science* **2014**, *344*, 1373–1377.

[61] Ge, Q.; Li, Z. Q.; Wang, Z. L.; Kowsari, K.; Zhang, W.; He, X. N.; Zhou, J. L.; Fang, N. X. Projection micro stereolithography based 3D printing and its applications. *Int. J. Extrem. Manuf.* **2020**, *2*, 022004.

[62] Choi, J. W.; Wicker, R. B.; Cho, S. H.; Ha, C. S.; Lee, S. H. Cure depth control for complex 3D microstructure fabrication in dynamic mask projection microstereolithography. *Rapid Prototyping J.* **2009**, *15*, 59–70.

[63] Sugioka, K.; Cheng, Y. Ultrafast lasers-reliable tools for advanced materials processing. *Light: Sci. Appl.* **2014**, *3*, e149.

[64] Cumpston, B. H.; Ananthavel, S. P.; Barlow, S.; Dyer, D. L.; Ehrlich, J. E.; Erskine, L. L.; Heikal, A. A.; Kuebler, S. M.; Lee, I. Y. S.; McCord-Maughon, D. et al. Two-photon polymerization initiators for three-dimensional optical data storage and microfabrication. *Nature* **1999**, *398*, 51–54.

[65] Zhou, W. H.; Kuebler, S. M.; Braun, K. L.; Yu, T. Y.; Cammack, J. K.; Ober, C. K.; Perry, J. W.; Marder, S. R. An efficient two-photon-generated photoacid applied to positive-tone 3D microfabrication. *Science* **2002**, *296*, 1106–1109.

[66] Fischer, J.; Wegener, M. Three-dimensional optical laser lithography beyond the diffraction limit. *Laser Photonics Rev.* **2013**, *7*, 22–44.

[67] Malinauskas, M.; Žukauskas, A.; Hasegawa, S.; Hayasaki, Y.; Mizeikis, V.; Buividas, R.; Juodkazis, S. Ultrafast laser processing of materials: From science to industry. *Light: Sci. Appl.* **2016**, *5*, e16133.

[68] Wang, H.; Zhang, W.; Ladika, D.; Yu, H. Y.; Gailevičius, D.; Wang, H. T.; Pan, C. F.; Nair, P. N. S.; Ke, Y. J.; Mori, T. et al. Two-photon polymerization lithography for optics and photonics: Fundamentals, materials, technologies, and applications. *Adv. Funct. Mater.* **2023**, *33*, 2214211.

[69] Xing, J. F.; Zheng, M. L.; Duan, X. M. Two-photon polymerization microfabrication of hydrogels: An advanced 3D printing technology for tissue engineering and drug delivery. *Chem. Soc. Rev.* **2015**, *44*, 5031–5039.

[70] Wang, H.; Wang, H. T.; Zhang, W.; Yang, J. K. W. Toward near-perfect diffractive optical elements via nanoscale 3D printing. *ACS Nano* **2020**, *14*, 10452–10461.

[71] Picard, M.; Mohanty, A. K.; Misra, M. Recent advances in additive manufacturing of engineering thermoplastics: Challenges and opportunities. *RSC Adv.* **2020**, *10*, 36058–36089.

[72] Yamada, A.; Niikura, F.; Ikuta, K. A three-dimensional microfabrication system for biodegradable polymers with high resolution and biocompatibility. *J. Micromech. Microeng.* **2008**, *18*, 025035.

[73] Malinauskas, M.; Farsari, M.; Piskarskas, A.; Juodkazis, S. Ultrafast laser nanostructuring of photopolymers: A decade of advances. *Phys. Rep.* **2013**, *533*, 1–31.

[74] Zhang, J.; Xiao, P. 3D printing of photopolymers. *Polym. Chem.* **2018**, *9*, 1530–1540.

[75] Fouassier, J. P.; Lalevée, J. *Photoinitiators for Polymer Synthesis: Scope, Reactivity, and Efficiency*; Wiley-VCH: Weinheim, 2012.

[76] Liu, H. L.; Wang, H. T.; Wang, H.; Deng, J.; Ruan, Q. F.; Zhang, W.; Abdelraouf, O. A. M.; Ang, N. S. S.; Dong, Z. G.; Yang, J. K. W. et al. High-order photonic cavity modes enabled 3D structural colors. *ACS Nano* **2022**, *16*, 8244–8252.

[77] Zhang, Y. S.; Khademhosseini, A. Advances in engineering hydrogels. *Science* **2017**, *356*, eaaf3627.

[78] Torgersen, J.; Ovsianikov, A.; Mironov, V.; Pucher, N.; Qin, X. H.; Li, Z. Q.; Cicha, K.; Machacek, T.; Liska, R.; Jantsch, V. et al. Photosensitive hydrogels for three-dimensional laser microfabrication in the presence of whole organisms. *J. Biomed. Opt.* **2012**, *17*, 105008.

[79] Wang, K. J.; Amin, K.; An, Z. S.; Cai, Z. X.; Chen, H.; Chen, H. Z.; Dong, Y. P.; Feng, X.; Fu, W. Q.; Gu, J. B. et al. Advanced functional polymer materials. *Mater. Chem. Front.* **2020**, *4*, 1803–1915.

[80] Ge, Q.; Sakhaei, A. H.; Lee, H.; Dunn, C. K.; Fang, N. X.; Dunn, M. L. Multimaterial 4D printing with tailorable shape memory polymers. *Sci. Rep.* **2016**, *6*, 31110.

[81] Xu, J.; Wang, X. W.; Wang, C. J.; Yuan, L.; Chen, W. J.; Bao, J. X.; Su, Q.; Xu, Z. H.; Wang, C. J.; Wang, Z. L. et al. A review on micro/nanoforming to fabricate 3D metallic structures. *Adv. Mater.* **2021**, *33*, 2000893.

[82] Wei, C.; Zhang, Z. Z.; Cheng, D. X.; Sun, Z.; Zhu, M. H.; Li, L. An overview of laser-based multiple metallic material additive manufacturing: From macro- to micro-scales. *Int. J. Extrem. Manuf.* **2021**, *3*, 012003.

[83] Vyatskikh, A.; Delalande, S.; Kudo, A.; Zhang, X.; Portela, C. M.; Greer, J. R. Additive manufacturing of 3D nano-architected metals. *Nat. Commun.* **2018**, *9*, 593.

[84] Xia, X. X.; Afshar, A.; Yang, H.; Portela, C. M.; Kochmann, D. M.; Di Leo, C. V.; Greer, J. R. Electrochemically reconfigurable architected materials. *Nature* **2019**, *573*, 205–213.

[85] Lian, J.; Jang, D.; Valdevit, L.; Schaedler, T. A.; Jacobsen, A. J.; B.Carter, W.; Greer, J. R. Catastrophic vs gradual collapse of thin-walled nanocrystalline Ni hollow cylinders as building blocks of microlattice structures. *Nano Lett.* **2011**, *11*, 4118–4125.

[86] Formanek, F.; Takeyasu, N.; Tanaka, T.; Chiyoda, K.; Ishikawa, A.; Kawata, S. Three-dimensional fabrication of metallic nanostructures over large areas by two-photon polymerization. *Opt. Express* **2006**, *14*, 800–809.

[87] Surjadi, J. U.; Feng, X. B.; Fan, R.; Lin, W. T.; Li, X. C.; Lu, Y. Hollow medium-entropy alloy nanolattices with ultrahigh energy absorption and resilience. *NPG Asia Mater.* **2021**, *13*, 36.

[88] Saccone, M. A.; Gallivan, R. A.; Narita, K.; Yee, D. W.; Greer, J. R. Additive manufacturing of micro-architected metals via hydrogel infusion. *Nature* **2022**, *612*, 685–690.

[89] Wang, Y. Y.; Yi, C. Q.; Tian, W. X.; Liu, F.; Cheng, G. J. Free-space direct nanoscale 3D printing of metals and alloys enabled by two-photon decomposition and ultrafast optical trapping. *Nat. Mater.* **2024**, *23*, 1645–1653.

[90] Cao, Y. Y.; Takeyasu, N.; Tanaka, T.; Duan, X. M.; Kawata, S. 3D metallic nanostructure fabrication by surfactant-assisted multiphoton-induced reduction. *Small* **2009**, *5*, 1144–1148.

[91] Jung, W.; Jung, Y. H.; Pikhitsa, P. V.; Feng, J. C.; Yang, Y.; Kim, M.; Tsai, H. Y.; Tanaka, T.; Shin, J.; Kim, K. Y. et al. Three-dimensional nanoprinting via charged aerosol jets. *Nature* **2021**, *592*, 54–59.

[92] Meza, L. R.; Das, S.; Greer, J. R. Strong, lightweight, and recoverable three-dimensional ceramic nanolattices. *Science* **2014**, *345*, 1322–1326.

[93] Vyatskikh, A.; Kudo, A.; Delalande, S.; Greer, J. R. Additive manufacturing of polymer-derived titania for one-step solar water purification. *Mater. Today Commun.* **2018**, *15*, 288–293.

[94] Sänger, J. C.; Pauw, B. R.; Riechers, B.; Zocca, A.; Rosalie, J.; Maaß, R.; Sturm, H.; Günster, J. Entering a new dimension in powder processing for advanced ceramics shaping. *Adv. Mater.* **2023**, *35*, 2208653.

[95] Wang, Y.; Yang, J.; Wang, Z. W.; Kong, X. F.; Sun, X. Y.; Tian, J. J.; Zhang, X. S.; Zhao, X. L.; Liu, Y. P.; Li, H. S. et al. The development and progression of micro-nano optics. *Front. Chem.* **2022**, *10*, 916553.

[96] Kotz, F.; Quick, A. S.; Risch, P.; Martin, T.; Hoose, T.; Thiel, M.; Helmer, D.; Rapp, B. E. Two-photon polymerization of nanocomposites for the fabrication of transparent fused silica glass microstructures. *Adv. Mater.* **2021**, *33*, 2006341.

[97] Wen, X. W.; Zhang, B. Y.; Wang, W. P.; Ye, F.; Yue, S.; Guo, H.; Gao, G. H.; Zhao, Y. S.; Fang, Q. Y.; Nguyen, C. et al. 3D-printed silica with nanoscale resolution. *Nat. Mater.* **2021**, *20*, 1506–1511.

[98] Cooperstein, I.; Indukuri, S. R. K. C.; Bouketov, A.; Levy, U.; Magdassi, S. 3D printing of micrometer-sized transparent ceramics with on-demand optical-gain properties. *Adv. Mater.* **2020**, *32*, 2001675.

[99] Kagan, C. R.; Lifshitz, E.; Sargent, E. H.; Talapin, D. V. Building devices from colloidal quantum dots. *Science* **2016**, *353*, aac5523.

[100] Liu, S. F.; Hou, Z. W.; Lin, L. H.; Li, F.; Zhao, Y.; Li, X. Z.; Zhang, H.; Fang, H. H.; Li, Z. C.; Sun, H. B. 3D nanoprinting of semiconductor quantum dots by photoexcitation-induced chemical bonding. *Science* **2022**, *377*, 1112–1116.

[101] Kovalenko, M. V.; Manna, L.; Cabot, A.; Hens, Z.; Talapin, D. V.; Kagan, C. R.; Klimov, V. I.; Rogach, A. L.; Reiss, P.; Milliron, D. J. et al. Prospects of nanoscience with nanocrystals. *ACS Nano* **2015**, *9*, 1012–1057.

[102] Issa, A.; Izquierdo, I.; Merheb, M.; Ge, D. D.; Broussier, A.; Ghabri, N.; Marguet, S.; Couteau, C.; Bachelot, R.; Jradi, S. One strategy for nanoparticle assembly onto 1D, 2D, and 3D polymer micro and nanostructures. *ACS Appl. Mater. Interfaces* **2021**, *13*, 41846–41856.

[103] Oran, D.; Rodriques, S. G.; Gao, R. X.; Asano, S.; Skylar-Scott, M. A.; Chen, F.; Tillberg, P. W.; Marblestone, A. H.; Boyden, E. S. 3D nanofabrication by volumetric deposition and controlled shrinkage of patterned scaffolds. *Science* **2018**, *362*, 1281–1285.

[104] Han, F.; Gu, S. Y.; Klimas, A.; Zhao, N.; Zhao, Y. X.; Chen, S. C. Three-dimensional nanofabrication via ultrafast laser patterning and kinetically regulated material assembly. *Science* **2022**, *378*, 1325–1331.

[105] Li, F.; Liu, S. F.; Liu, W. Y.; Hou, Z. W.; Jiang, J. X.; Fu, Z.; Wang, S.; Si, Y. L.; Lu, S. Y.; Zhou, H. W. et al. 3D printing of inorganic nanomaterials by photochemically bonding colloidal nanocrystals. *Science* **2023**, *381*, 1468–1474.

[106] Lyu, X.; Zheng, Z. Q.; Shiva, A.; Han, M.; Dayan, C. B.; Zhang, M. C.; Sitti, M. Capillary trapping of various nanomaterials on additively manufactured scaffolds for 3D micro-/nanofabrication. *Nat. Commun.* **2024**, *15*, 6693.

[107] Pan, C.; Han, Y. F.; Lu, J. P. Design and optimization of lattice structures: A review. *Appl. Sci.* **2020**, *10*, 6374.

[108] Bauer, J.; Hengsbach, S.; Tesari, I.; Schwaiger, R.; Kraft, O. High-strength cellular ceramic composites with 3D microarchitecture. *Proc. Natl. Acad. Sci. USA* **2014**, *111*, 2453–2458.

[109] Kang, Y. L.; Zhao, J.; Zeng, Y.; Du, X.; Gu, Z. Z. 3D printing photonic crystals: A review. *Small* **2024**, *20*, 2403525.

[110] Halir, R.; Bock, P. J.; Cheben, P.; Ortega-Moñux, A.; Alonso-Ramos, C.; Schmid, J. H.; Lapointe, J.; Xu, D. X.; Wangüemert-Pérez, J. G.; Molina-Fernández, Í. et al. Waveguide sub-wavelength structures: A review of principles and applications. *Laser Photonics Rev.* **2015**, *9*, 25–49.

[111] Choudhury, S. M.; Wang, D.; Chaudhuri, K.; DeVault, C.; Kildishev, A. V.; Boltasseva, A.; Shalaev, V. M. Material platforms for optical metasurfaces. *Nanophotonics* **2018**, *7*, 959–987.

[112] Gan, Z. S.; Turner, M. D.; Gu, M. Biomimetic gyroid nanostructures exceeding their natural origins. *Sci. Adv.* **2016**, *2*, e1600084.
[113] Liu, Y. J.; Wang, H.; Ho, J.; Ng, R. C.; Ng, R. J. H.; Hall-Chen, V. H.; Koay, E. H. H.; Dong, Z. G.; Liu, H. L.; Qiu, C. W. et al. Structural color three-dimensional printing by shrinking photonic crystals. *Nat. Commun.* **2019**, *10*, 4340.
[114] Cansoy, C. E.; Erbil, H. Y.; Akar, O.; Akin, T. Effect of pattern size and geometry on the use of Cassie-Baxter equation for superhydrophobic surfaces. *Colloid. Surf. A: Physicochem. Eng. Asp.* **2011**, *386*, 116–124.
[115] Ge, P.; Wang, S. L.; Zhang, J. H.; Yang, B. Micro-/nanostructures meet anisotropic wetting: From preparation methods to applications. *Mater. Horiz.* **2020**, *7*, 2566–2595.
[116] Bixler, G. D.; Bhushan, B. Fluid drag reduction with shark-skin riblet inspired microstructured surfaces. *Adv. Funct. Mater.* **2013**, *23*, 4507–4528.
[117] Tricinci, O.; Terencio, T.; Mazzolai, B.; Pugno, N. M.; Greco, F.; Mattoli, V. 3D micropatterned surface inspired by *Salvinia molesta* via direct laser lithography. *ACS Appl. Mater. Interfaces* **2015**, *7*, 25560–25567.
[118] Bunea, A. I.; Szczotka, N.; Navne, J.; Taboryski, R. Single-step fabrication of superhydrophobic surfaces by two-photon polymerization micro 3D printing. *Micro Nano Eng.* **2023**, *19*, 100192.
[119] Blasco, E.; Müller, J.; Müller, P.; Trouillet, V.; Schön, M.; Scherer, T.; Barner-Kowollik, C.; Wegener, M. Fabrication of conductive 3D gold-containing microstructures via direct laser writing. *Adv. Mater.* **2016**, *28*, 3592–3595.
[120] Yan, D. J.; Chang, J. H.; Zhang, H.; Liu, J. X.; Song, H. L.; Xue, Z. G.; Zhang, F.; Zhang, Y. H. Soft three-dimensional network materials with rational bio-mimetic designs. *Nat. Commun.* **2020**, *11*, 1180.
[121] Shen, Z. M.; Hu, X. N.; Tang, Z. J.; Xiao, Y.; Wang, S. H.; Cheng, X.; Zhang, Y. H. Curvature programming of freestanding 3D mesostructures and flexible electronics based on bilayer ribbon networks. *J. Mech. Phys. Solids* **2024**, *191*, 105766.
[122] Skylar-Scott, M. A.; Gunasekaran, S.; Lewis, J. A. Laser-assisted direct ink writing of planar and 3D metal architectures. *Proc. Natl. Acad. Sci. USA* **2016**, *113*, 6137–6142.
[123] Chen, C.; Wang, X.; Wang, Y.; Yang, D. D.; Yao, F. Y.; Zhang, W. X.; Wang, B.; Sewvandi, G. A.; Yang, D. S.; Hu, D. W. Additive manufacturing of piezoelectric materials. *Adv. Funct. Mater.* **2020**, *30*, 2005141.
[124] Chen, Z. H.; Chen, F. L.; Tu, Z. N.; Jiang, Q. C.; Wang, Y. Q.; Liu, X. Y.; Sheng, S. Microstructure-property relationships in piezoelectric-polymer composites: A review. *J. Polym. Res.* **2025**, *32*, 41.
[125] Jiao, P. C.; Egbe, K. J. I.; Xie, Y. W.; Matin Nazar, A.; Alavi, A. H. Piezoelectric sensing techniques in structural health monitoring: A state-of-the-art review. *Sensors* **2020**, *20*, 3730.
[126] Bodkhe, S.; Turcot, G.; Gosselin, F. P.; Therriault, D. One-step solvent evaporation-assisted 3D printing of piezoelectric PVDF nanocomposite structures. *ACS Appl. Mater. Interfaces* **2017**, *9*, 20833–20842.
[127] Jin, D. D.; Zhang, L. Collective behaviors of magnetic active matter: Recent progress toward reconfigurable, adaptive, and multifunctional swarming micro/nanorobots. *Acc. Chem. Res.* **2022**, *55*, 98–109.
[128] Zhou, Y.; Ye, M.; Hu, C. Z.; Qian, H. H.; Nelson, B. J.; Wang, X. P. Stimuli-responsive functional micro-/nanorobots: A review. *ACS Nano* **2023**, *17*, 15254–15276.
[129] Liu, J. M.; Zhuang, R. C.; Zhou, D. K.; Chang, X. C.; Li, L. Q. Design and manufacturing of micro/nanorobots. *Int. J. Extrem. Manuf.* **2024**, *6*, 062006.
[130] Gardi, G.; Ceron, S.; Wang, W. D.; Petersen, K.; Sitti, M. Microrobot collectives with reconfigurable morphologies, behaviors, and functions. *Nat. Commun.* **2022**, *13*, 2239.
[131] Richards, C. A.; Ocier, C. R.; Xie, D. J.; Gao, H. B.; Robertson, T.; Goddard, L. L.; Christiansen, R. E.; Cahill, D. G.; Braun, P. V. Hybrid achromatic microlenses with high numerical apertures and focusing efficiencies across the visible. *Nat. Commun.* **2023**, *14*, 3119.
[132] Marini, M.; Nardini, A.; Martínez Vázquez, R.; Conci, C.; Bouzin, M.; Collini, M.; Osellame, R.; Cerullo, G.; Kariman, B. S.; Farsari, M. et al. Microlenses fabricated by two-photon laser polymerization for cell imaging with non-linear excitation microscopy. *Adv. Funct. Mater.* **2023**, *33*, 2213926.
[133] Webber, D.; Zhang, Y. J.; Sampson, K. L.; Picard, M.; Lacelle, T.; Paquet, C.; Boisvert, J.; Orth, A. Micro-optics fabrication using blurred tomography. *Optica* **2024**, *11*, 665.
[134] Hsu, L. Y.; Melo, S. G.; Vazquez-Martel, C.; Spiegel, C. A.; Ziebert, F.; Schwarz, U. S.; Blasco, E. Alignment and actuation of liquid crystals via 3D confinement and two-photon laser printing. *Sci. Adv.* **2024**, *10*, eadq2597.
[135] Kim, J. B.; Chae, C.; Han, S. H.; Lee, S. Y.; Kim, S. H. Direct writing of customized structural-color graphics with colloidal photonic inks. *Sci. Adv.* **2021**, *7*, eabj8780.
[136] Demirörs, A. F.; Poloni, E.; Chiesa, M.; Bargardi, F. L.; Binelli, M. R.; Woigk, W.; De Castro, L. D. C.; Kleger, N.; Coulter, F. B.; Sicher, A. et al. Three-dimensional printing of photonic colloidal glasses into objects with isotropic structural color. *Nat. Commun.* **2022**, *13*, 4397.
[137] Xu, K. L.; Huang, B. Y.; Zhang, X. F.; Ge, S. S.; Wei, X. X. 3D printed flexible piezoelectric sensor with enhanced performance for gait recognition. *ACS Appl. Electron. Mater.* **2025**, *7*, 6015–6026.
[138] Xu, B. Y.; Yang, M. Y.; Cheng, W. J.; Li, X. Y.; Xu, X. M.; Li, W. M.; Zhang, H.; Zhou, M. Precision aerosol-jet micropatterning of liquid metal for high-performance flexible strain sensors. *Nat. Commun.* **2025**, *16*, 7920.
[139] Roy, S.; Deo, K. A.; Lee, H. P.; Soukar, J.; Namkoong, M.; Tian, L. M.; Jaiswal, A.; Gaharwar, A. K. 3D printed electronic skin for strain, pressure and temperature sensing. *Adv. Funct. Mater.* **2024**, *34*, 2313575.
[140] Ahmadipour, M.; Damacet, P.; Xiang, C. H.; Mirica, K. A.; Montazami, R. Smart textile: Electrohydrodynamic jet printing of ionic liquid-functionalized $Cu_3(HHTP)_2$ metal-organic frameworks for gas-sensing applications. *ACS Appl. Mater. Interfaces* **2025**, *17*, 12425–12439.
[141] Chen, C. C.; Fu, Y. H.; Sparks, S. S.; Lyu, Z. Y.; Pradhan, A.; Ding, S. C.; Boddeti, N.; Liu, Y.; Lin, Y. H.; Du, D. et al. 3D-printed flexible microfluidic health monitor for *in situ* sweat analysis and biomarker detection. *ACS Sens*. **2024**, *9*, 3212–3223.
[142] Song, Y.; Tay, R. Y.; Li, J. H.; Xu, C. H.; Min, J. H.; Shirzaei Sani, E.; Kim, G.; Heng, W. Z.; Kim, I.; Gao, W. 3D-printed epifluidic electronic skin for machine learning-powered multimodal health surveillance. *Sci. Adv.* **2023**, *9*, eadi6492.
[143] Dadras-Toussi, O.; Khorrami, M.; Louis Sam Titus, A. S. C.; Majd, S.; Mohan, C.; Abidian, M. R. Multiphoton lithography of organic semiconductor devices for 3D printing of flexible electronic circuits, biosensors, and bioelectronics. *Adv. Mater.* **2022**, *34*, 2200512.
[144] Waghule, T.; Singhvi, G.; Dubey, S. K.; Pandey, M. M.; Gupta, G.; Singh, M.; Dua, K. Microneedles: A smart approach and increasing potential for transdermal drug delivery system. *Biomed. Pharmacother.* **2019**, *109*, 1249–1258.
[145] Dervisevic, M.; Harberts, J.; Sánchez-Salcedo, R.; Voelcker, N. H. 3D polymeric lattice microstructure-based microneedle array for

transdermal electrochemical biosensing. *Adv. Mater.* **2024**, *36*, 2412999.

[146] Yang, J.; Gong, X.; Zheng, Y.; Duan, H.; Chen, S. J.; Wu, T.; Yi, C. Q.; Jiang, L. L.; Haick, H. Microneedle-based integrated pharmacokinetic and pharmacodynamic evaluation platform for personalized medicine. *Nat. Commun.* **2025**, *16*, 6260.

[147] Palagi, S.; Fischer, P. Bioinspired microrobots. *Nat. Rev. Mater.* **2018**, *3*, 113–124.

[148] Tottori, S.; Zhang, L.; Qiu, F. M.; Krawczyk, K. K.; Franco-Obregón, A.; Nelson, B. J. Magnetic helical micromachines: Fabrication, controlled swimming, and cargo transport. *Adv. Mater.* **2012**, *24*, 811–816.

[149] Mahkam, N.; Aghakhani, A.; Sheehan, D.; Gardi, G.; Katzschmann, R.; Sitti, M. Acoustic streaming-induced multimodal locomotion of bubble-based microrobots. *Adv. Sci.* **2023**, *10*, 2304233.

[150] Ceylan, H.; Yasa, I. C.; Yasa, O.; Tabak, A. F.; Giltinan, J.; Sitti, M. 3D-printed biodegradable microswimmer for theranostic cargo delivery and release. *ACS Nano* **2019**, *13*, 3353–3362.

[151] Cabanach, P.; Pena-Francesch, A.; Sheehan, D.; Bozuyuk, U.; Yasa, O.; Borros, S.; Sitti, M. Zwitterionic 3D-printed non-immunogenic stealth microrobots. *Adv. Mater.* **2020**, *32*, 2003013.

[152] Smart, C. L.; Pearson, T. G.; Liang, Z. X.; Lim, M. X.; Abdelrahman, M. I.; Monticone, F.; Cohen, I.; McEuen, P. L. Magnetically programmed diffractive robotics. *Science* **2024**, *386*, 1031–1037.

[153] Su, L.; Jin, D. D.; Wang, Y. Q.; Wang, Q. L.; Pan, C. F.; Jiang, S.; Yang, H. J.; Yang, Z. X.; Wang, X.; Xia, N. et al. Modularized microrobot with lock-and-detachable modules for targeted cell delivery in bile duct. *Sci. Adv.* **2023**, *9*, eadj0883.

[154] Urso, M.; Ussia, M.; Peng, X.; Oral, C. M.; Pumera, M. Reconfigurable self-assembly of photocatalytic magnetic microrobots for water purification. *Nat. Commun.* **2023**, *14*, 6969.

[155] Shen, Z. M.; Zhu, D. F.; Zhang, M. C. Synergy of smart materials and structures toward intelligent metamaterials. *SmartSys* **2025**, *1*, e70007.